Low Dose Interpolated Average CT for Thoracic PET/CT Attenuation Correction

by

Sun Tao

A thesis submitted in partial fulfillment of the requirements for the degree of

Master of Science In Electrical and Computer Engineering

Faculty of Science and Technology
University of Macau

2013

Approved by _____
Supervisor

_____

_____

_____

Date _____

In presenting this thesis in partial fulfillment of the requirements for a Master's degree at the University of Macau, I agree that the Library and the Faculty of Science and Technology shall make its copies freely available for inspection. However, reproduction of this thesis for any purposes or by any means shall not be allowed without my written permission. Authorization is sought by contacting the author at

Address:

Telephone:
Fax:
E-mail:

Signature _____

Date _____

University of Macau

Abstract

LOW DOSE INTERPOLATED AVERAGE CT FOR
THORACIC PET/CT ATTENUATION CORRECTION

by Sun Tao

Thesis Supervisor: Dr. Greta, Seng Peng Mok
Electrical and Computer Engineering

Positron emission tomography (PET) detects γ-ray emitted from the radioactive tracers injected in patient body via position sensitive detectors. The 3-dimensional (3D) activity distribution of the radiotracers can be obtained by image reconstruction of the raw data. On the other hand, computed tomography (CT) detects the attenuation coefficients of the patient body using x-ray. It provides relatively high-resolution image of the patient anatomy. Integrated PET/CT scanner provides medical, technical and economic merits as compared to standalone modalities.

Researchers have been striving to improve the PET/CT technology over a decade, including detectors, image reconstruction algorithms and image analysis. All these endeavors aim for the better image quality and quantitation, with lower radiation dose. Attenuation correction using CT data is the most important correction in PET and is critical for improving image quality and quantitation. However, respiratory motion is generally considered to be one of the main factors which degrade the image quality in CT-based attenuation correction.

This thesis aims to develop a new PET/CT attenuation correction method to reduce the respiratory motion misalignments between PET and CT and improve the PET quantitation. The first chapter of this thesis introduces the basic principle of PET/CT instrumentation, its role in detecting thoracic tumors, attenuation correction and respiratory misalignments in PET/CT. In the second chapter, several existing categories of the misalignment reduction methods are reviewed. The third chapter describes our proposed attenuation correction method, including theory, software and hardware implementation. The computer simulation and clinical study to evaluate our

method are discussed in chapter 4 and 5 respectively. The conclusion and future work are demonstrated in the end of this thesis.

TABLE OF CONTENTS

LIST OF FIGURES

Number *Page*

LIST OF TABLES

Number *Page*

LIST OF ABBREVIATIONS

2/3/4 D	2/3/4- Dimensional
ABC	Active Breathing Controller
AC	Attenuation Correction
ACF	Attenuation Correction Factor
CACT	Cine Average CT
CMOS	Complementary Metal-Oxide-Semiconductor
CT	Computed Tomography
DIBH	Deep-Inspiration Breath-Hold
FDG	Fluorodeoxyglucose
FFD	Free-Form Deformation
FOV	Field-of-View
HCT	Helical CT
IACT	Interpolated Average CT
IDE	Integrated Development Environment
IO	Input-Output
ITK	Insight Segmentation and Registration Toolkit
LOR	Line-of-Response
MBK	Motion Blurring Kernel
MEMS	Microelectromechanical System
MI	Mutual Information
NMSE	Normalized Mean Square Error
NSCLC	Non-Small Cell Lung Cancer
NSD	Normalized Standardized Deviation
OFM	Optical Flow Method
OPL-EM	One-Pass List-mode Expectation Maximization
OS-EM	Ordered Subsets Expectation Maximization
PET	Positron Emission Tomography
PVE	Partial Volume Effect

ROI	Region-of-Interest
RPM	Real-time Position Management
SCLC	Small Cell Lung Cancer
SD	Standard Deviation
SNR	Signal-to-Noise Ratio
STIR	Software for Tomographic Image Reconstruction
SUV	Standardized Uptake Value
TBR	Target-to-Background Ratio
VOI	Volume-of-Interest
XCAT	Digital 4D Extended Cardiac Torso

ACKNOWLEDGMENTS

The author wishes to thank my supervisor Dr. Greta, Mok Seng Peng, for her guidance and support during my master study. She brought me a most advanced medical imaging research topic and provided numerous resources to help me accomplish the project. She is enthusiastic at research and surely I learned a lot from her. She is always willing to help me read the manuscripts and reply my questions.

I am very grateful to Prof. Wu Tung-Hsin from National Yang-Ming University who made our clinical experiments possible. He kindly helped my living when I was in Taiwan. I would like to thank Wu Nien-Yun, Dr. Yang Bang-Hung, Dr. Wang Shyh-Jen from Taipei Veterans General Hospital for their clinical support and advice. I also want to thank Guan Yu-Xiang from National Yang-Ming University for his assistance on experiment setup.

I would like to thank Prof. Vai Mang-I, Dr. Wan Feng, Pedro Mou from Department of Electrical and Computer Engineering in University of Macau for their advices. Special thanks to all my colleagues in Biomedical Imaging Lab and my friends. It is great to have fun with you in Macau.

DEDICATION

I wish to dedicate this thesis to my parents: Zhao Xiao Feng and Sun Yi Yi.

CHAPTER 1 : INTRODUCTION

In 2000, Time Magazine honored Positron Emission Tomography/Computed Tomography (PET/CT) as the “Medical Science Invention of the Year” for its novelty of combining anatomical and functional imaging to enhance diagnostic accuracy, which has been proven in staging of cancer, especially non-small cell lung cancer. In this chapter, we will introduce the background and significance of lung cancer, PET/CT instrumentation, attenuation correction and the respiratory misalignments in PET/CT.

1.1 LUNG CANCER

Lung cancer is a disease caused by the rapid, abnormal growth and division of cells in lung tissue. In last decades, lung cancer causes more deaths than any other cancer in the world, which accounts for 14% of all cancers and 28% of all cancer deaths every year in the United States [1]. For therapeutic, biological and pathological reasons, lung cancers are divided into two major groups: small cell lung cancer (SCLC) and non-small cell lung cancer (NSCLC). These two groups make up more than 90% of all lung cancer cases. NSCLC is more common and usually locates in the periphery of the lung [2], while SCLC is far more aggressive than NSCLC [3]. Only 10% lung cancer is diagnosed in the early stage while most of the cancers are detected in the later stages due to the nature of this tumor, which do not produce any discomfort until they have grown to a large size. Survival from lung cancer is highly dependent on the staging of disease, which determines the surgical efficacy: the more advance the stage, the less favorable is the individual’s prognosis. This thesis proposes a method to improve the detection and quantification of the lung tumors using the PET/CT technique, which will in turn improve the staging accuracy or the treatment monitoring.

1.2 INSTRUMENTATION

1.2.1 POSITRON EMISSION TOMOGRAPHY (PET)

The process of positron emission and followed positron-electron annihilation in PET imaging is shown in Figure 1.1. Pairs of photons with energy of 511 keV travel ~180 ° and leave the subject. A pair of position sensitive detectors records the photons as a coincident event in a straight line which is known as line-of-response (LOR). The raw data is a sinogram, i.e., distance-angle histogram, which records the sum of LORs detected by each pair of detectors. A 3-dimensional (3D) image of radiotracer distribution can then be obtained by analytical or statistical reconstruction algorithms.

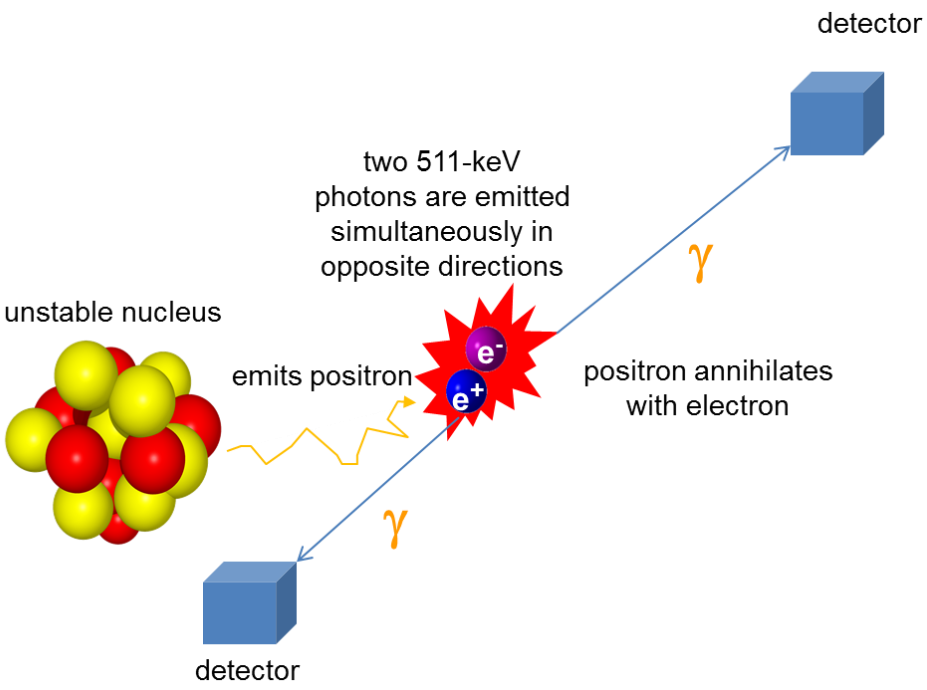

Figure 1.1 Process of positron emission and positron-electron annihilation

For PET imaging, a positron-emitting radionuclide is attached to a chemical compound to form a biological radiotracer, which is injected into the subject and accumulate in regions-of-interest (ROIs). The most commonly used PET tracer at present is ^{18}F-FDG, which is a kind of glucose analogue, i.e., fluorodeoxyglucose,

labeled with positron-emitting isotope ^{18}F. Its accumulation in tissue is proportional to the amount of glucose utilization, and increased consumption of glucose is a characteristic of most cancers. Positrons are emitted and further interact with electrons to generate pairs of annihilated gamma rays which are 511 keV and ~180° apart. Position sensitive detectors are used to detect the emitted gamma rays (Figure 1.1).

PET allows *in vivo* quantification of radioactivity concentrations to estimate glucose uptake of tumors. Standardized uptake value (SUV) measurement on PET images is the most common approach to estimate the glucose utilization rate. It is defined as a ratio of tissue radioactivity concentration of FDG (KBq/ml) measured in a ROI at time T divided by the injected dose (KBq) per body weight (kg):

$$\mathrm{SUV(T)} = \frac{Activity\ Concentration\ (KBq/ml\ )}{Injected\ dose\ (KBq)/Body\ weight\ (kg)}$$

The SUV can be used to differentiate tumors to be malignant or benign, classify disease stage, and monitor the treatment response to the tumors.

1.2.2 POSITRON EMISSION TOMOGRAPHY /COMPUTED TOMOGRAPHY (PET/CT)

Before PET/CT, physicians preferred examining both PET and CT images side by side to identify and locate tumors or other anomalies. Integrated PET/CT scanners perform both scans in one session without moving the patient from one scanner to another. Intrinsically fused PET and CT images from PET/CT provide more accurate lesion localization and characterization than separate PET and CT images. Studies indicated that PET/CT improves the staging of disease in non-small cell lung cancer and lymph node cancer [4].

There are several commercial PET/CT scanners from different vendors nowadays. Figure 1.2A shows a standard GE STE PET/CT scanner (GE Medical Systems, Milwaukee, WI, USA). The PET gantry of a GE STE PET/CT scanner has 13440 4.7×6.3×30 mm detector crystals and has a transaxial field-of-view (FOV) of 70 cm. The CT component of this scanner has a 50-cm transaxial FOV. In general, a

PET/CT scanner consists of three main components (Figure 1.2B): (1) a CT gantry (2) a PET gantry, and (3) a patient bed. In a typical PET/CT protocol, patients first receive a CT scan and then a PET scan while the patient bed moves axially into the scanner. The operator initiates a whole-body scout CT scan (2–10 s) to determine a scan region. Then a whole-body helical CT (HCT) scan (30 s – 2 mins) is conducted. The last step is the PET scan (5–45 minutes). The patient stays still on the bed throughout these 3 acquisitions. All patient data can be acquired in 3D mode and are corrected for attenuation, random, scatter, and dead time effects. The final reconstructed images will be obtained by different algorithms such as 3D ordered-subset expectation maximization (OS-EM).

A

B

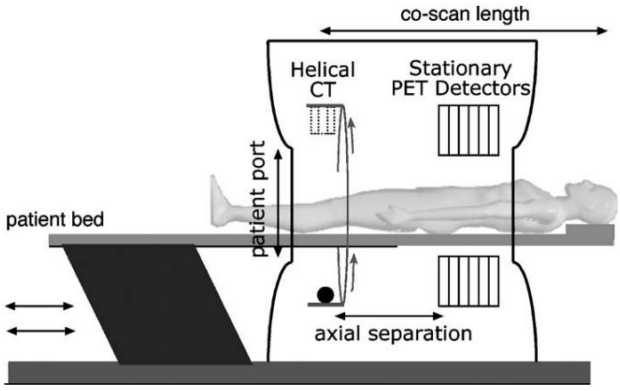

Figure 1.2 Standard PET/CT scanner and its diagram

1.3 ATTENUATION CORRECTION IN PET/CT

For medical radionuclide imaging, the emitted gamma rays are attenuated in the body mainly via photoelectric absorption and Compton scattering before reaching the detectors. This effect is more prominent for tracers with lower energy and for regions with higher attenuation coefficients, e.g. bone and metallic implants. Meanwhile, the photons originated from the center of the object would be more likely to be attenuated as compared to those arisen from the periphery. Thus, this effect is proportional to patient body sizes and would contribute to gradual decrease of activity towards the center of the body. Attenuation correction (AC) is the most important correction in PET and critical for improving image quality and quantitation.

1.3.1 ATTENUATION CORRECTION FOR STANDALONE PET

Initial efforts of AC in emission tomography include conjugate-counting techniques, e.g., using the geometric mean of the conjugate projections [5] and the Chang's multiplicative method [6]. Both methods assume a constant attenuation coefficient across the patient body. The attenuation correction factor (ACF) can be obtained by estimating the body thickness from the preliminary uncorrected images. Although this is a reasonable estimate for brain and abdomen, this assumption is not suitable for most other complex regions like thorax and pelvis. An additional transmission scan can be used to address the calculation of the ACFs in the regions with the presence of air and bone.

AC on the standalone PET was performed mostly with an external ^{68}Ge 511-keV pin source that rotated around the patient before the combined PET/CT scanner was invented. Transmission images were acquired to obtain the ACFs to correct the PET sinogram before image reconstruction. The scan took ~15-30 minutes and the reconstructed image using the ^{68}Ge usually showed significantly high noise. The pre-injection transmission scan required patients to stay on the bed of the scanner before the emission acquisition, which limited the patients' throughput. If the patients underwent the transmission scan after the tracer injection, the photons emitted from the patients could interfere with the transmission acquisition and degrade the count rate performance of the detectors. The limited count rate of this transmission scan

may substantially affect the quantitative accuracy or cause artifacts in the emission data [7]. The anatomical information provided by the transmission scan was also limited and was not suitable for diagnostic purpose.

1.3.2 CT-BASED ATTENUATION CORRECTION

Nowadays, most commercial PET/CT scanners perform X-ray CT-based AC [8]. CT transmission scans produce huge number of photons even at low CT tube current. Since CT-based AC ensures the significant energy difference between the X-rays (~30-120 keV) and gamma-rays (511 keV), the transmission scan would not be contaminated by the emitted gamma-rays from the patients. Thus, the CT scan can be done after the tracer injection. However, it is necessary to transform the CT transmission images acquired from an integrated energy spectrum of ~30-120 keV to monoenergetic attenuation maps of 511 keV for AC of the emission data. This conversion usually involves segmentation of different tissues or applying the bilinear scaling methods [9, 10]. The use of CT-based attenuation maps leads to a more accurate activity concentration values, better uniformity [11] and provides more anatomical information for the correspondingly registered emission data.

1.4 RESPIRATORY MISALIGNMENTS BETWEEN PET & CT

On the other hand, CT-based attenuation corrected PET image is hampered by artifacts that are usually not seen in the PET images corrected by the ^{68}Ge transmission scan. Examples are misalignments and artifacts due to respiratory motion [12-14], truncation [15], metallic implants [16, 17] and CT contrast agents [18, 19]. Respiratory motion is generally considered to be the biggest problem in CT-based AC among all factors. For standalone diagnostic CT, the optimized protocol is to perform a 3D helical CT (HCT) scan of the thoracic cavity over a single full-inspiration breath-hold. When applied for PET AC, this technique captures a snapshot of the thorax at a certain respiratory phase and does not represent the time-averaged position of the thorax as PET acquisition does.

This misalignment between transmission and emission scan is most noticeable at the left lung, especially for two regions: (i) structures around lower thorax and

diaphragm, where the transmission scan may not be present in the emission scan (Figure 1.3A); (ii) structures around the lung and left-ventricle interface, where myocardial uptake is prominent overlying the left lung of the CT in the fused images (Figure 1.4A). One study indicated that more than 40% of the studies have misalignments between the measured and the true position around the thoracic structures [20] when no corrections were performed. These PET/CT mismatch artifacts may lead to inaccurate localization of tumors and hence potential misdiagnoses [13, 21, 22].

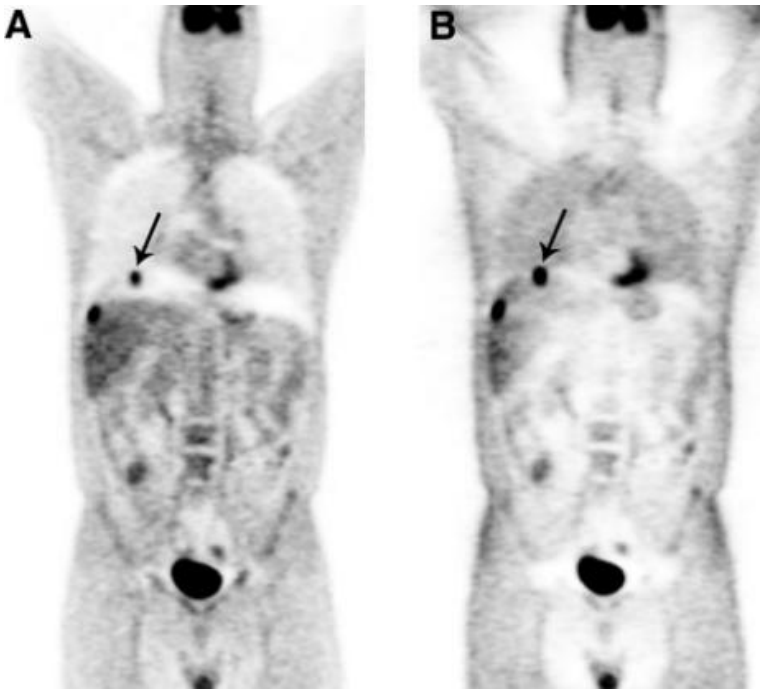

Figure 1.3 (A) A lesion at the dome of liver was mislocalized to right lung (arrow) because of the respiratory motion. (B) Images without AC showed that all lesions were confined to the liver. (Image courtesy of Sureshbabu W et al. [14])

A B

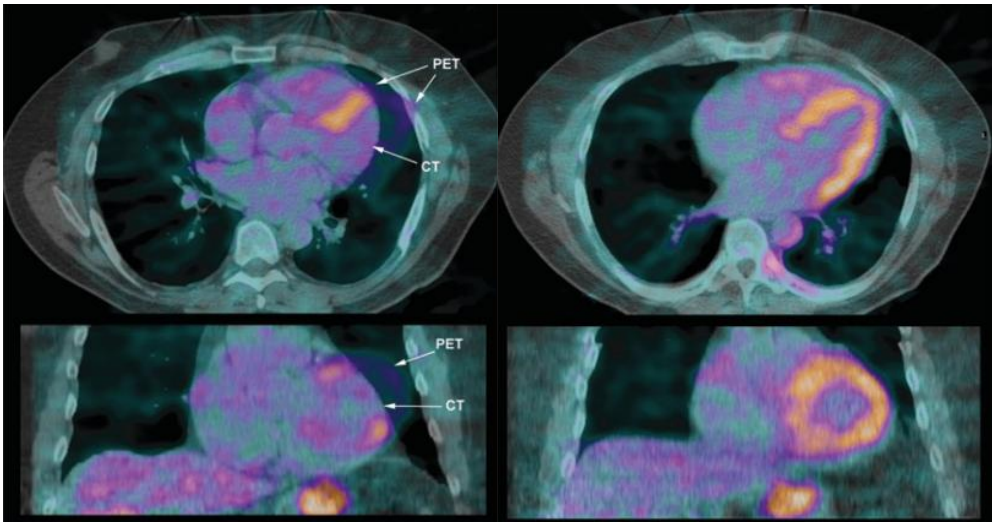

Figure 1.4 (A) HCT and PET fusion images in transaxial (top) and coronal (bottom) views showed marked mis-registration. Arrows indicated the mismatch of heart borders between the HCT and PET images, and an artifactual defect in the myocardium. (B) For the same patient, cine average CT and PET fusion images showed no mis-registration and artifactual defects. (Image courtesy of Gould KL et al. [20])

CHAPTER 2 : REVIEW OF EXISTING METHODS FOR RESPIRATORY ARTIFACTS REDUCTION

Four categories of PET/CT respiratory artifact reduction methods are listed below: (i) Breathing instruction based methods [23, 24]; (ii) CT protocol based methods [25-27]; (iii) Gated 4-dimensional (4D) PET/CT [28-33] and (iv) Deconvolution PET [34, 35].

2.1 BREATHING INSTRUCTION BASED METHODS

2.1.1 SHALLOW BREATHING

Instead of the deep-inspiration breath-hold protocol in diagnostic CT, some studies acquired both CT and PET under continuously shallow breathing state, which had relatively smaller motion amplitudes. A study, however, showed that this protocol resulted in an unsatisfactory evaluation of the lung parenchyma on CT images where subcentimeter nodules can be missed to cause inaccurate comprehensive cancer staging [36]. Nowadays, multi-detector CT technology that employs 6 or more detector rows can reduce magnitude and frequency of respiratory artifacts in free breathing PET/CT [37]. The irregular breathing pattern will be significantly mitigated because of the shorten whole-body CT scan time with the multi-detector CT technology.

2.1.2 NORMAL END-EXPIRATION BREATH-HOLD

Some researchers believed normal end-expiration breath-hold is the optimal breathing maneuver for transmission scan in thoracic PET/CT [24, 38]. This CT protocol reduced the occurrence and the severity of respiratory artifacts on co-registered PET/CT images. Juan *et al.* showed that reconstructed images from patients of normal-expiration breath-hold group had 28% less incidence rate of artifacts as compared to those from the free-breathing group [38]. In the meantime, AC using

maximal-inspiration breath-hold protocol resulted in more serious underestimation of SUV especially when breathing amplitude increased [39]. One possible explanation for the positive results of normal end-expiration breath-hold CT is that a normal human spends most time in expiration in a whole respiratory cycle.

However, patient's compliance and comfort is the clinical challenge of normal end-expiration breath-hold protocol. Even for the most advanced multi-detector CT scanner, some patients are incapable of maintaining breath-hold for the duration of the whole-body CT scan. On the other hand, Hamill *et al*. [39] indicated good SUV recovery of normal end-expiration breath-hold was actually due to canceling effects between SUV underestimation from motion blurring and overestimation from attenuation. For small lung tumors near the diaphragm, their phantom study showed the inaccurate estimation of SUV after AC with normal end-expiration CT.

2.1.3 DEEP-INSPIRATION BREATH-HOLD (DIBH) PET/CT

Nehmeh *et al.* proposed a deep-inspiration breath-hold protocol for both CT and PET (DIBH PET/CT) acquisition [40]. The whole process was shown in Figure 2.1. The patient was instructed to breathe deeply and then hold the breath, under the monitoring with an amplitude gating device. Firstly, breath-hold helical CT data were acquired for about 16 s. PET scan was divided to nine 20 s frames, i.e., with a total acquisition of 3 mins for one bed position (Figure 2.1). In the beginning of each PET frame, patient was instructed to breathe and hold the breath again as in DIBH CT. The breath-hold signal exhibited a relaxation period before it stabilized. Therefore, it was necessary to wait for 1–2 s before starting the acquisition. This method showed an increase in lesion SUV of as much as 83% and a reduction in the distance between the centroids of PET and CT lesions as much as 49%, compared to the deep-inspiration breath-hold CT method. Similar results were found by Meirelles *et al.*[41] and Torizuka *et al.* [42].

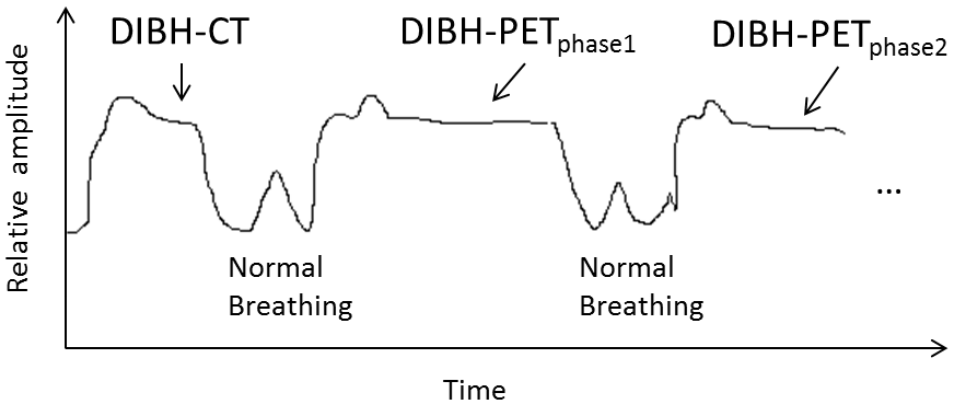

Figure 2.1 Breathing signals of a patient undergoing DIBH PET/CT

By now the DIBH PET/CT method was only explored in lung lesion studies. In reality, even a single breath-hold for 20 s may not be acceptable for senior patients or patients with underlying lung diseases such as emphysema or pulmonary fibrosis [42]. Unsuccessful breath-hold due to irregular breathing pattern may cause highly variable results, which will affect the diagnostic accuracy. Also, additional external monitoring and breathe-coaching are needed to measure the respiratory cycle to ensure the matching between the transmission and the emission data of different respiratory phases.

2.2 CT PROTOCOL BASED METHODS

There are two main scan modes for CT acquisition, the axial (step-and-shoot) mode and the helical (spiral) mode. The step-and-shoot mode consists of two steps: (i) The patient remain stationary while the X-ray tube and gantry rotate around the patient to acquire a complete set of projections at a prescribed scanning location; (ii) The X-ray tube is off and the patient is translated to the next prescribed axial scanning location. The duty cycle (scan time/total time) of the step-and-shoot CT is ~50% at best. The HCT was then introduced to solve the interscan missing problem as in the step-and-shoot CT [43, 44]. The CT data are acquired while the patient is continuously transported through the gantry with a constant speed. This will guarantee

the duty cycle to be near 100%. The scanner is able to image a given volume in a shorter time as compared to the step-and-shoot mode, since the scanning speed performance is substantially improved.

Specific CT protocols based on the axial mode or helical mode have been proposed for AC in PET images, with the same idea to acquire CT data over multiple respiratory cycles to ensure the CT attenuation map matches with the PET. Thus, breathing-induced artifacts such as PET/CT spatial mismatch, target blurring and underestimation of the SUV would be reduced.

2.2.1 SLOW CT

Lagerwaard *et al.* introduced low-rotation CT under helical mode to average several respiratory cycles over the scan duration [45]. Pitch was set to 1 and the tube rotation time of a single slice CT was slowed down to 4 s/rot. Compared to the diagnostic deep-inspiration breath-hold CT, low-rotation CT was closer to the average position of the thoracic cavity structures in PET.

Instead of changing the rotation time, another way to slow down the CT scan is to decrease the pitch. Nye *et al.* set the pitch to be 0.562 which was the lowest possible value in the scanner [46]. This pitch value increased the axial sampling during free-breathing mode without increasing the tube rotation time. A total of 16 s scan was used to cover the chest cavity. Final CT data were matched with the PET slice thickness for AC and to suppress respiratory motion artifacts. One concern for low-pitch CT is the radiation burden. Due to the potential longer exposure time, higher radiation dose is delivered to the patients.

2.2.2 CINE AVERAGE CT (CACT)

The 4-dimensional CT (4D CT) under cine mode provides images of all phases of the breathing cycle for tumor staging and radiation therapy treatment planning [47]. Cine mode technique, modified from step-and-shoot mode, acquired repeated axial CT images at each table position for a certain time period. This method produced even thinner slice thickness than those of a low-pitch helical scan.

Pan *et al.* [26], Gould *et al.*[20] and Cook *et al.* [48] averaged the images of all phases in 4D CT to form a CACT at each table position (Figure 2.2) to cover the whole thorax region. The acquisition time for each table position is 5.9 s. The average CT of the thorax can then be combined with the HCT data of the regions outside the thorax, e.g., abdomen, to make up the integrative whole body CT images. This method greatly improved the registration accuracy and tumor SUV as compared to the AC using deep-inspiration or normal end-expiration breath-hold HCTs.

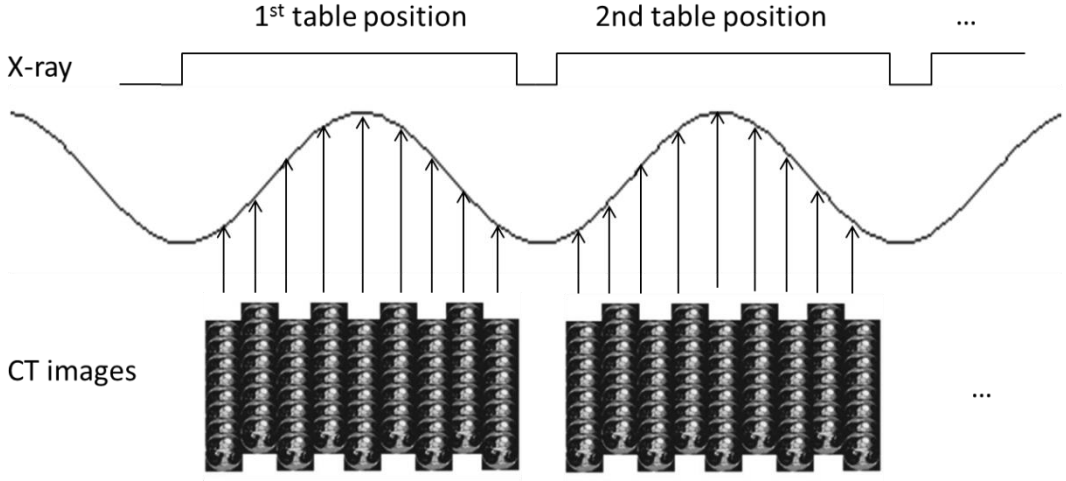

Figure 2.2 Scheme to generate 4D CT

2.3 GATED 4D PET/CT

The aforementioned methods aimed to correct the misalignments between PET and CT by modifying the CT images to match with the PET images. However, respiratory motion blur always exists in the static PET, and it cannot be compensated by only matching the CT with the static PET images. The following techniques aimed to reduce the PET/CT misalignment artifacts and correct the motion blurring by further processing the PET raw data or reconstructed images.

Respiratory gated PET was firstly proposed for brain PET scan to remove patient motions [49]. To reduce smearing due to the breathing motions and improve quantification of ^{18}F-FDG uptake in lung lesions, Nehmeh *et al.* proposed respiratory gated PET [50]. Before, each gated PET image was usually directly corrected by an unsynchronized breath-hold CT. However, the reconstructed image quality in some

frames is even worse than those of the non-gated PET with AC by a conventional breath-hold CT. In principle, 4D PET/CT should apply phase-matched CT for AC on gated PET images. In synchrony with the externally monitored breathing signal such as from the real-time position management (RPM, Varian Medical Systems, Palo Alto, CA, Figure 2.3) [50], respiratory gated PET data were acquired into discrete bins. 4D CT data were acquired and sorted according to their phases to generate a respiratory gated CT data. To make the CT images of each phase coincide with the PET images, the gated CT images were then spatially re-binned and re-sliced in the axial direction. The gated PET data can then be corrected for attenuation with the corresponding gated CT data.

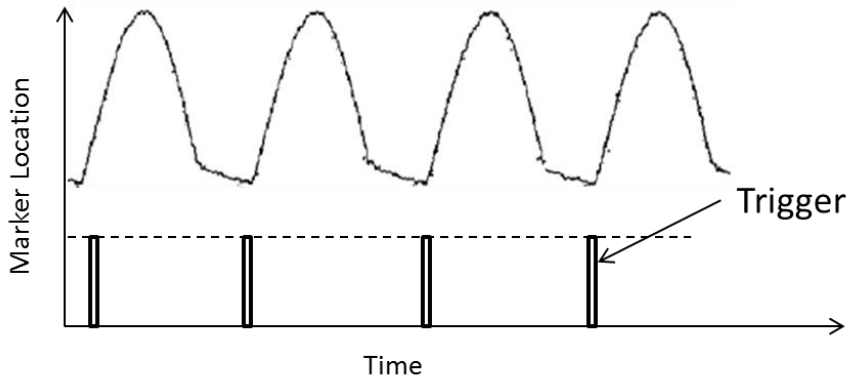

Figure 2.3 Respiratory gating signals indicated by RPM marker location and the corresponding electrical triggers for PET acquisition.

2.3.1 REGISTRATION-BASED METHODS

One may notice that in 4D PET/CT, each PET bin only contains a small fraction of detected PET events. The resultant reconstructed images from one bin, therefore, have a high noise level and a poor signal-to-noise ratio (SNR). In principle, it is better to utilize all PET information from the whole respiratory cycle instead of only one phase. One method to achieve this is to transform each respiratory PET bin to a referenced target bin that corresponds optimally to a matched CT phase from the gated CT data before AC (Figure 2.4). Thus, PET images can be reconstructed using information

from the complete dataset.

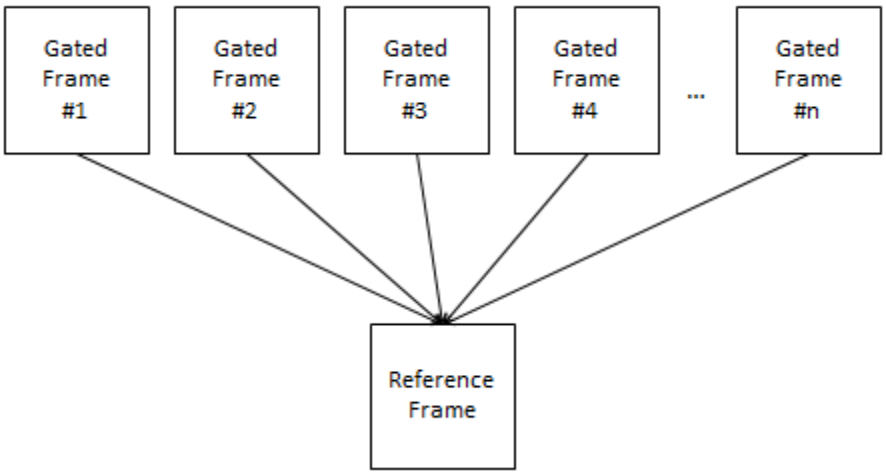

Figure 2.4 4D registration-based PET/CT gated schemes

Lung motion due to respiration is non-rigid in nature, and the deformation amplitude of the lungs during respiration is larger than that of the heart. As shown in the previous chapter, CT attenuation maps are not always co-registered to PET images especially at the lower thorax and diaphragm where large deformations often happen, which will lead to inaccurate PET reconstructed images. Non-rigid motion correction algorithms, therefore, would be superior to rigid motion correction algorithms for registration in lung imaging. The motion vectors can be derived from gated CT and/or gated PET for the registration.

Dawood *et al.* used the optical flow method (OFM) to calculate 3D motion vectors from the gated PET images [51]. OFM was used for estimating motion vectors between any bin and the target bin. The reconstructed image contained all PET information with minimal motion, leading to more accurate AC. Thorndyke *et al.* proposed a retrospective stacking method for gated PET image processing [52]. All the gated PET images were retrospectively grouped into several bins along measured amplitude of the respiratory cycle from RPM. These bins were registered one-by-one to a referenced bin through B-spline deformable transformation and then stacked and averaged to form a composite image. This method yielded reduced blurring and increased SNR in the reconstructed images as compared to conventional

non-registration-based gated 4D PET/CT. The improvement of contrast slightly varied for lung lesion of different locations and sizes [39]. This was likely due to the fact that smaller lesions (7 and 11 mm) are more likely to suffer from partial volume effect (PVE) as compared to the bigger lesions [53, 54].

The 4D PET/CT transform algorithm for registration is very computationally intensive and requires gating hardware to support the image acquisition. This method may not be feasible for most clinics currently because of the high complexity of implementation.

2.3.2 RECONSTRUCTION-BASED METHODS

Motion compensation can also be done by incorporating deformations information among different frames into the iterative reconstruction process. The reconstruction-based method is proven to provide superior image quality than the registration-based method.

Lamare *et al*.[55] indicated the elastic motion correction can be integrated into the system matrix in the PET reconstruction process. If P is the system matrix that describes the PET system, the data acquisition in PET can be represented by the following equation:

$$m = Pf \tag{2.1}$$

where m are the measured datasets and f is the radioactive distribution at the reference respiratory location. The 3D spatial transformations for correcting the respiratory motion were obtained from the simulated 4D CT data. Deformation matrices were derived among all individual frames (acquired at time t) and the referenced frame of the end exhalation (acquired at time t_0). Then Equation 2.1 can be represented as:

$$m_t = P_t f \tag{2.2}$$

where m_t are the measured datasets at variable time t, P_t are system matrices at variable time t, and f is the radioactive distribution at time t_0. This elastic-based

respiratory motion correction can be integrated into the one-pass list-mode expectation maximization (OPL-EM) algorithm:

$$f^{k+1} = \frac{f^k}{S} \sum_N P_t^T \frac{1}{P_t f^k} \quad (2.3)$$

where *S* is the sensitivity image used to correct for attenuation and normalization. *N* is the number of temporally gated frames.

The results showed that, in comparison to registering the reconstructed images to the reference image, incorporating the spatial transformation into reconstruction led to a superior contrast of 20%~30% in the recovered lesion. Thus, motion-free PET images at end-expiration would be obtained after the AC with the end-expiration CT data. Incorporating motion compensation into 4D reconstruction can yield a better trade-off between SNR and bias in estimating the activity for moving tumor than non-gated and gating without registration methods [29]. Similar results were also demonstrated in [56, 57].

2.4 DECONVOLUTION PET/CT

Deconvolution techniques could reduce the inherent motion blur in PET images without any gating. This technique have been utilized successfully to remove the blurring of medical images, such as CT [58], MRI [59] and solve the PVE problem in PET [60, 61].

Naqa *et al.* suggested that the motion blur of the lung lesion can be modeled as an convolution between the true PET image and the local motion blurring kernel (MBK) [34]:

$$I_{obs} = I_{true} \otimes MBK \quad (2.7)$$

where I_{obs} was the observed blurred PET image, I_{true} was the true PET image to be estimated, $\otimes$ represented the convolution process. There were three steps for their method: (i) Estimation of the breathing motion model from 4D CT data; (ii)

Conversion of the motion estimates into the MBK; (iii) Deconvolution based on an expectation-maximization iterative algorithm with the estimated MBK. The preliminary clinical results showed this method was promising for either large or small tumors. This method, however, required 4D CT to generate the MBK, which may impose additional radiation burden.

There are three limitations for respiratory motion deblurring with deconvolution method: (i) Deconvolution works on the average reconstructed image but not on phase by phase images. If the tumor moved in a non-rigid way, which sometimes happens, the over- or underestimation in tumor activity concentration can lead to inaccurate PET image quantification. (ii) This method is applied at a regional level but not for the entire image. It can only correct the motion blur in a tumor-related region rather than the whole PET image since most body structures move with a different pattern as compared to the tumor. (iii) Deconvolution process generally amplifies image noise thus may affect image quality and quantitative accuracy.

2.5 DISCUSSION

Each respiratory artifact reduction technique has its own advantages and disadvantages and the optimum approach may probably be application- or patient-dependent. While improving image quality is important, the actual implementation of the respiratory artifact reduction technique highly depends on the robustness and complexity of the clinical set up. Their merits and disadantages are summarized in Table 2.1.

Table 2.1 Summary of different PET/CT respiratory artifacts reduction techniques

	Description	**Advantages**	**Disadvantages**
Breathing instructions	Specialized breath-hold CTs	Relatively simple implementation, respiratory monitoring device is needed sometimes	Successful implementation highly depends on patients' compliance
CT protocol based	CACT; slow CT; low-pitch CT	No respiratory monitoring is needed	High dose; artifacts from irregular respiration
4D respiratory gating	Phase-by-phase CT to correct corresponding phase-by-phase PET	Further reduces motion blurring	High complexity of implementation
Deconvolution	Deconvoling the PET to match CT	Independent from hardware	Region-based correction

CHAPTER 3 : INTERPOLATED AVERAGE CT

We proposed an interpolated average CT (IACT) method for improved AC in PET/CT. Similar to the CT protocol based method in Table 2.1, we generate attenuation image from CT that is similar to CACT to match with the PET image, with relatively low dose. In this chapter, we discuss the details about the theory and working principles for IACT.

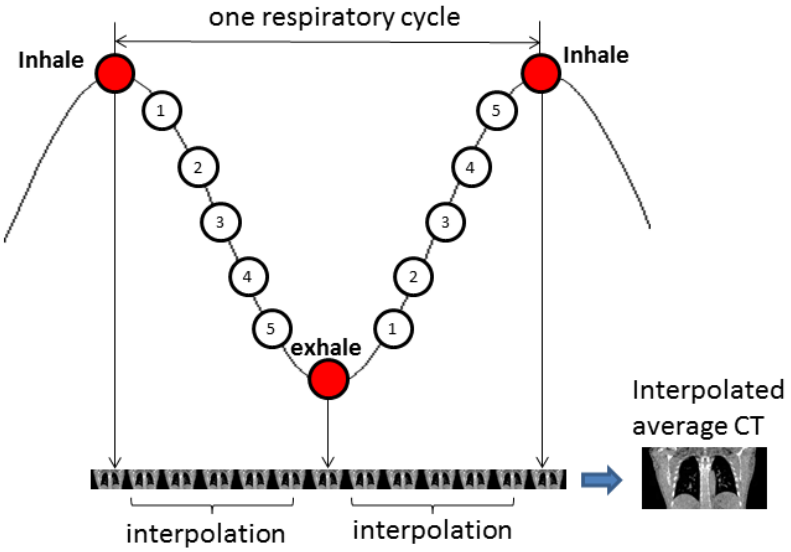

Figure 3.1 Steps to generate IACT.

According to Figure 3.1, assuming that the extreme phases of end-inspiration and end-expiration CT images are captured, we can calculate the velocity matrix between them by deformable registration, and later perform the interpolation according to an empirical or patient-specific function. After that, we average the intensity of the original extreme and interpolated images to generate IACT. There are three steps for the actual implementation: Step 1: Calculating the velocity matrix; Step 2: Interpolation; Step 3: Averaging.

3.1 CALCULATING THE VELOCITY MATRIX

Deformable image registrations are performed based on two acquired extreme phases, i.e., end-inspiration and end-expiration.

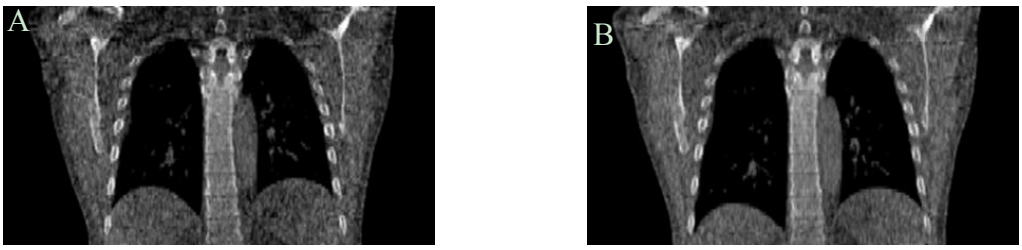

Figure 3.2 (A) End-expiration and (B) end-inspiration image

The end-expiration image is used as the fixed image and the end-inspiration is used as the moving image (Figure 3.2). We set the velocity matrix V as the deformation vector for each voxel:

$$\mathrm{V}: \mathrm{F}(\mathrm{x}, \mathrm{y}, \mathrm{z}) \longrightarrow \mathrm{M}(\mathrm{x}', \mathrm{y}', \mathrm{z}') \tag{3.1}$$

which maps every point in the "moving image" M into its corresponding point in the "fixed image" F. The V matrix is what needs to be estimated. In the following session, we will discuss two different algorithms: (i) optical flow method (OFM) and (ii) B-spline method to obtain V.

Method 1: Optical flow method (OFM)

OFM estimates the V based on a vector which describes the displacement per voxel. We assume the intensity values of F and M images remain the same during the motion:

$$I(x, y, z, t) = I(x + \delta x, y + \delta y, z + \delta z, t + \delta t) \tag{3.2}$$

Applying Taylor series to the above equation:

$$I(x+\delta x,\ y+\delta y,\ z+\delta z,\ t+\delta t) = I(x,y,z,t) + \frac{\partial I}{\partial x}\delta x + \frac{\partial I}{\partial y}\delta y + \frac{\partial I}{\partial z}\delta z + \frac{\partial I}{\partial t}\delta t + H \quad (3.3)$$

where *H* is the higher order term which is small enough to be ignored. Dividing both sides of Equation 3.3 by δt:

$$\frac{\partial I}{\partial x}u + \frac{\partial I}{\partial y}v + \frac{\partial I}{\partial z}w + \frac{\partial I}{\partial t} = 0 \quad (3.4)$$

or

$$I_x u + I_y v + I_z w + I_t = 0 \quad (3.5)$$

where *u*, *v*, *w* are the *x*, *y* and *z* components of the velocity $\vec{V}$. $I_x = \frac{\partial I}{\partial x}, I_y = \frac{\partial I}{\partial y}, I_z = \frac{\partial I}{\partial z}, I_t = \frac{\partial I}{\partial t}$ are the derivatives of the image at (x,y,z,t) directions. (u,v,w) is the optical flow of the image.

The Equation 3.5 has three unknowns and cannot be solved. Horn/Schunck proposed using gradient descent method with a global smoothing function to solve the equation [62]. The smoothing term was given as:

$$||\nabla u||^2 + \left|\left|\nabla v\right|\right|^2 + \left|\left|\nabla w\right|\right|^2 = u_x^2 + u_y^2 + u_z^2 + v_x^2 + v_y^2 + v_z^2 + w_x^2 + w_y^2 + w_z^2 \quad (3.6)$$

where the Laplacian operator $\nabla^2 = \frac{\partial^2}{\partial x^2} + \frac{\partial^2}{\partial y^2} + \frac{\partial^2}{\partial z^2}$.

A cost function to be minimized is then given by:

$$f = \int \left(\left(I_x u + I_y v + I_z w + I_t\right)^2 + \alpha(||\nabla u||^2 + ||\nabla v||^2 + ||\nabla w||^2)\right) dxdydz \quad (3.7)$$

where α is a regularization constant. Larger value of α will lead to a smoother flow. We set it as an empirical value of 5 in the further simulation experiment [63]. To minimize$f$, according to the Euler-Lagrange equations, Equation 3.7 will become to:

$$\begin{aligned} I_x\left(I_x u + I_y v + I_z w + I_t\right) - \alpha^2\nabla^2 u = 0 \\ I_y\left(I_x u + I_y v + I_z w + I_t\right) - \alpha^2\nabla^2 v = 0 \\ I_z\left(I_x u + I_y v + I_z w + I_t\right) - \alpha^2\nabla^2 w = 0 \end{aligned} \quad (3.8)$$

Then the Laplacian of u can be approximated by $\nabla^2 u \approx \vec{u} - u$ where $\vec{u}$ is the mean of u in the $3 \times 3 \times 3$ neighborhood voxels of the current point position. Likewise, $\nabla^2 v \approx \vec{v} - v$ and $\nabla^2 w \approx \vec{w} - w$:

$$\begin{aligned} I_x\left(I_x u + I_y v + I_z w + I_t\right) - \alpha^2(\bar{u} - u) = 0 \\ I_y\left(I_x u + I_y v + I_z w + I_t\right) - \alpha^2(\bar{v} - v) = 0 \\ I_z\left(I_x u + I_y v + I_z w + I_t\right) - \alpha^2(\bar{w} - w) = 0 \end{aligned} \tag{3.9}$$

In matrix form:

$$\begin{bmatrix} I_x^2 + \alpha^2 & I_x I_y & I_x I_z \\ I_x I_y & I_y^2 + \alpha^2 & I_y I_z \\ I_x I_z & I_y I_z & I_z^2 + \alpha^2 \end{bmatrix} \begin{bmatrix} u \\ v \\ w \end{bmatrix} = \begin{bmatrix} -I_x I_t + \alpha^2 \bar{u} \\ -I_y I_t + \alpha^2 \bar{v} \\ -I_z I_t + \alpha^2 \bar{w} \end{bmatrix}$$

(3.10)

Use of Cramer's rule and Jacobi iteration leads to the following update rules:

$$\begin{aligned} u^{(k+1)} &= \bar{u}^{(k)} - \frac{I_x\left[I_x \bar{u}^{(k)} + I_y \bar{v}^{(k)} + I_z \bar{w}^{(k)} + I_t\right]}{I_x^2 + I_y^2 + I_z^2 + \alpha^2} \\ v^{(k+1)} &= \bar{v}^{(k)} - \frac{I_y\left[I_x \bar{u}^{(k)} + I_y \bar{v}^{(k)} + I_z \bar{w}^{(k)} + I_t\right]}{I_x^2 + I_y^2 + I_z^2 + \alpha^2} \\ w^{(k+1)} &= \bar{w}^{(k)} - \frac{I_z\left[I_x \bar{u}^{(k)} + I_y \bar{v}^{(k)} + I_z \bar{w}^{(k)} + I_t\right]}{I_x^2 + I_y^2 + I_z^2 + \alpha^2} \end{aligned} \tag{3.11}$$

The velocity $\vec{V} = (u, v, w)$ can then be calculated by employing an iterative gradient descent technique which steps in the direction of the gradient vector.

Method 2: B-spline method

B-spline is an algorithm applied to calculate the deformation vectors in deformable image registration based on the Insight Segmentation and Registration Toolkit (ITK) [64]. The deformation vectors include lateral, anterior-posterior and inferior-superior displacement for each voxel on two CT volumes, i.e., end-inspiration and end-expiration phases in our study. Instead of directly estimating the deformation

vector V, this method features a transformation function described by several parameters. In B-spline method, deformation field V consists of a global field and a local field:

$$\mathrm{V}(\mathrm{x},\mathrm{y},\mathrm{z}) = V_{global}(x,y,z) + V_{local}(x,y,z) \tag{3.12}$$

For the global field, one choice is a rigid transformation which is parameterized by 6 degrees of freedom, describing the rotations and translations. A more general class of transformation is affine transformation, which has 6 additional degrees of freedom, additionally describing scaling and shearing. In 3D operation, the affine transformation can be written as:

$$V_{global}(x,y,z) = \begin{pmatrix} \theta_{11} & \theta_{12} & \theta_{13} \\ \theta_{21} & \theta_{22} & \theta_{23} \\ \theta_{31} & \theta_{32} & \theta_{33} \end{pmatrix} \begin{pmatrix} x \\ y \\ z \end{pmatrix} + \begin{pmatrix} \theta_{14} \\ \theta_{24} \\ \theta_{34} \end{pmatrix} \tag{3.13}$$

where the coefficients of θ parameterize the 12 degrees of freedom.

For the local field, it is difficult to describe the local deformation via parameterized transformation. Instead, a free-form deformation (FFD) based on cubic B-spline is chosen. The basic idea of FFD is to deform an object by manipulating an underlying mesh of control points which are uniformly spaced to cover the moving image. The resulting deformation controls the shape of the 3D object and produces a smooth and continuous transformation:

$$V_{local}(x,y,z) = \sum_{i=0}^{3}\sum_{j=0}^{3}\sum_{k=0}^{3} B_i B_j B_k \, \phi_{ijk} \tag{3.14}$$

where B is the corresponding basis function in each dimension, ϕ_{ijk} is the control lattice as the local transformation parameter.

Later a sum of the square difference C between the fixed image and moving image is calculated as the similarity index between 2 images:

$$C_{similarity} = \frac{1}{N}\sum_{i}^{N}(A_i - B_i)^2 \tag{3.15}$$

where N is the total number of voxels. To find the optimal deformation, we minimize a cost function associated with the global transformation parameters Θ, as well as the local transformation parameters Φ.

$$C(\Theta, \Phi) = C_{similarity}(I, I + V) \tag{3.16}$$

To increase the smoothness of the deformation field, we introduce a regularization term of C_{smooth} [65, 66]:

$$C_{smooth} = \frac{1}{v}\int_0^X \int_0^Y \int_0^Z \left[\left(\frac{\partial^2 V}{\partial x^2}\right)^2 + \left(\frac{\partial^2 V}{\partial y^2}\right)^2 + \left(\frac{\partial^2 V}{\partial z^2}\right)^2 + 2\left(\frac{\partial^2 V}{\partial xy}\right)^2 + 2\left(\frac{\partial^2 V}{\partial xz}\right)^2 + 2\left(\frac{\partial^2 V}{\partial yz}\right)^2\right] dx\, dy\, dz \tag{3.17}$$

where V denotes the volume of the image. Hence the cost function can be written as:

$$C(\Theta, \Phi) = C_{similarity}\left(I, I + V_{global} + V_{local}\right) + \lambda C_{smooth}(V) \tag{3.18}$$

here, λ is the weighting factor which defines the tradeoff between the alignment of two image volumes and the smoothness of the transformation. It is set to be 0.01 because it provides a good compromise between the two competing terms of the cost function.

Note that the regularization term is zero for any affine transformations and, therefore, penalizes only non-affine transformations [67]. Deformation field V can be changed to:

$$C(\Theta, \Phi) = C_{similarity}\left(I, I + V_{global} + V_{local}\right) + \lambda C_{smooth}(V_{local}) \tag{3.19}$$

There are two sub-steps to find the transformation parameters. A single affine registration is first performed while its transformation parameters Θ are optimized. Then B-spline registration is performed and the transformation parameters Φ are determined while minimizing the cost function. The algorithm stops if a local optimum of the cost function has been found. The forward local transformation parameters Φ_{ie} are calculated from end-inspiration phase to end-expiration phase and backward local transformation parameters Φ_{ei} are calculated vice versa. With global and local parameters found in Equation 3.19, the deformation field V for every voxel from the moving image to the fixed image can be estimated.

We compared these two deformable registration methods in the later simulation study. The method with superior registration accuracy and reconstructed image quality would be used in the clinical study.

3.2 INTERPOLATION

Interpolated phases are obtained via linear or sinusoidal functions based on the velocity matrix. In the simulation study, the function used for interpolation [68] is listed in Figure 3.3 and Equation 3.20:

Figure 3.3 Respiratory volume change in one respiratory cycle.

$$V(t) = \begin{cases} -250cos\left(\frac{\pi}{2}t\right) + 250 & 0 \le t \le 2 \\ -250cos\left(\frac{\pi}{3}(5-t)\right) + 250 & 2 \le t \le 5 \end{cases} \tag{3.20}$$

ϕ_{ie} is divided based on *V(t)* to obtain the interpolated deformation fields. Thus, we can generate interpolated phases #2, #3, #4 and #5 (Figure 3.1) by warping the original end-expiration phase (#1) based on ϕ_{ie}. Similarly, phases #7, #8, #9, #10, #11 and #12 are warped from the end-inspiration phase (#6) based on ϕ_{ei}. In the clinical study, a more realistic upper liver movement function (Figure 3.4 & Equation 3.21) was used for interpolation [69]:

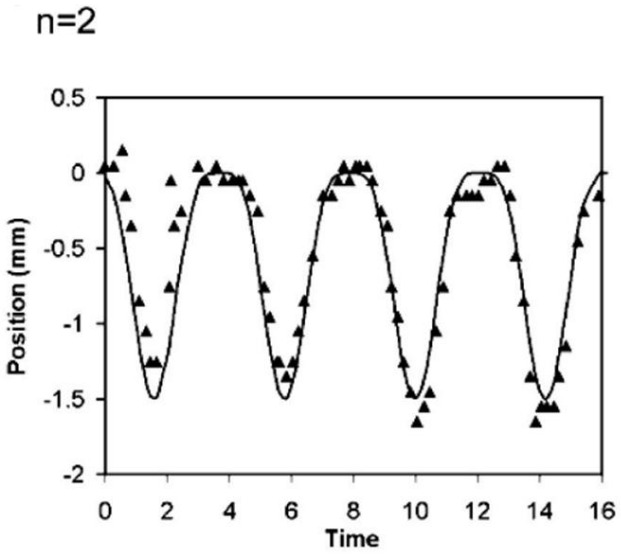

Figure 3.4 Sample empirical upper liver movement function.

$$z(t) = z_0 - b\cos^{2n}(\pi t/\tau) \tag{3.21}$$

The *n* defines degree of the asymmetry that patients tend to spend more breathing time over expiration as compared to inspiration. It was adjusted according to each patient's respiratory signal in the clinical study.

3.3 AVERAGING

The final IACT is generated by averaging the intensity of the interpolated and original extreme phases (Figure 3.1). The IACT was then be used for AC in PET images in the simulation and clinical study. More implementation details and applications about Ch. 3.2 and Ch. 3.3 were discussed in the later chapters.

CHAPTER 4 : SIMULATION STUDY

We performed a simulation study to evaluate the performance of IACT for different motion amplitudes, noise levels and robustness of the proposed method [70].

4.1 MATERIALS AND METHODS

4.1.1 4D EXTENDED CARDIAC TORSO (XCAT) PHANTOM

To investigate the effectiveness of IACT for PET/CT AC, we utilized the digital 4D Extended Cardiac Torso (XCAT) phantom (Figure 4.1A) that realistically models the anatomy, activity distribution of a male patient injected with ^{18}F-FDG and the respiratory motions. Three maximum respiratory diaphragm motions of 2 cm, 3 cm and 4 cm were modeled (Figure 4.2). Starting from the end-inspiration phase, one respiratory cycle was divided into 13 phases (Figure 4.1B). A 25 mm-diameter spherical lesion with target-to-background ratio (TBR) of 4:1 was placed at the base of the right lung, where the respiratory motion is most prominent.

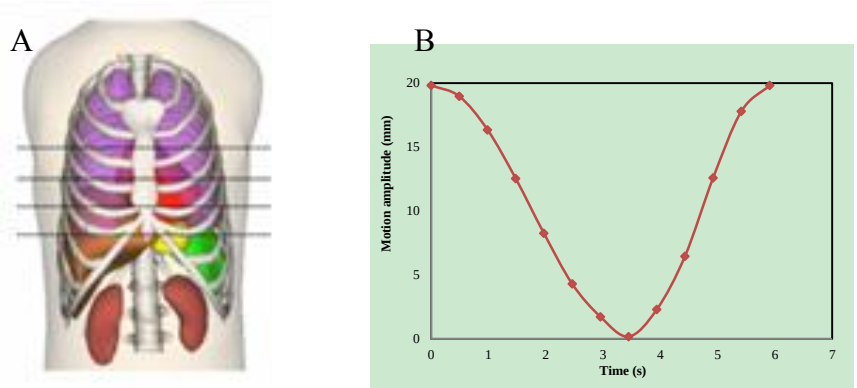

Figure 4.1 (A) XCAT phantom and (B) its sampled respiratory cycle

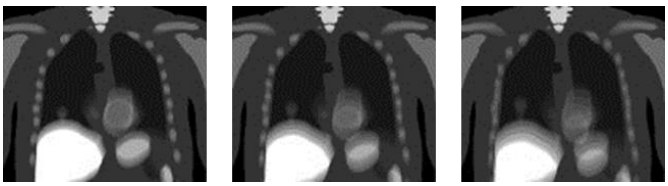

Figure 4.2 The average activity maps from left to right: 2 cm, 3 cm, 4 cm

4.1.2 SIMULATION DESIGNS

We used the analytical projector and Ordered Subsets Expectation Maximization (OS-EM) reconstruction algorithm provided by STIR (Software for Tomographic Image Reconstruction) [71], modeling a GE Discovery STE PET scanner. STIR is a open source object-oriented library implemented in C++ for 3D tomographic imaging. Its emphasis is on image reconstruction in PET and other image modalities. Investigating the design of new scanner systems can use this tool to reconstruct either simulated or acquired data with existing algorithms such that they can concentrate on the most desirable design.

Three bed positions were simulated to cover the whole thoracic region in PET. The average of the 13 phases of the activity maps was used to generate the sinogram to represent static PET acquisition with average of a respiratory cycle.

For noise-free data, the CACT was represented by the average of the 13 phases of the attenuation maps as the gold standard. The HCT, which is usually a snapshot of a respiration cycle, was represented by phase #1 (end-inspiration phase), #5 (mid-respiratory phase) or #8 (end-expiration phase) (HCT-1, HCT-5 and HCT-8) of the attenuation maps.

The IACT was generated by averaging the original phases and the interpolated phases obtained from the OFM method, while B-spline method was also evaluated for the maximum motion amplitude. Three different IACTs were simulated: (1) 2 original extreme phases + 11 interpolated phases ($IACT_{2o}$), (2) 2 original phases right after the end-inspiration and -expiration phases + 11 interpolated phases ($IACT_{2s}$); and (3) 4 original phases (2 extreme and 2 mid-respiratory phases) + 9 interpolated phases ($IACT_{4o}$). The $IACT_{2s}$ represented the slight mis-capturing, i.e., “shifted version”, of

the 2 extreme phases, which might happen in the real clinical situation. The PET images were reconstructed by OS-EM algorithm with AC of HCTs, IACTs, and CACT respectively in STIR.

For noisy simulation, data were then generated by adding Poisson noise based on a count level of ~9.5 M, representing 20 mins whole body PET acquisition. CT projections were generated from different AC maps using an analytical projector provided by STIR and then added with Gaussian noise, which was based on the standard deviation (SD) of a ROI drawn in the liver region on the clinical CT patient data [63]. The projections were reconstructed with filtered back-projection method to get the reconstructed CT images with similar noise level as in the clinical CT data for further AC in PET.

4.1.3 DATA ANALYSIS

The reconstructed PET images from different AC schemes were compared with the original phantom based on visual assessment and analyzed in terms of the following indices:

(i) Normalized mean square error (NMSE)

The whole reconstructed volume was used to assess the average NMSE as compared to the original phantom.

$$\text{average NMSE} = \frac{1}{m}\sum_{j=1}^{m}\left(\frac{x_j}{\bar{x}} - \frac{\lambda_j}{\bar{\lambda}}\right)^2 \tag{4.1}$$

where m is the number of voxels in the whole reconstructed volume, λ is the voxel count value in the original phantom, $\bar{\lambda}$ is the mean voxel value of the original phantom, x is the voxel count value in the noise free and noisy reconstructed images, $\bar{x}$ is the mean voxel value of the reconstructed images and j is the voxel index.

(ii) Mutual information (MI)

The normalized MI ($I(X, Y)$) between X and Y, a measure of the statistical

dependence between 2 variables, was applied to estimate the nonlinear image intensity distribution between IACTs/HCTs/CACT and the original phantom:

$$\mathrm{I}(X,Y) = \frac{P(X)+P(Y)}{P(X,Y)} \tag{4.2}$$

where X and Y are two random variables, i.e., two different CT images in our case, $P(X)$ is the histogram of X, $P(Y)$ is the histogram of Y and $P(X, Y)$ is the joint histogram of X and Y.

(iii) Target-to-background ratio (TBR)

The 3D TBR was calculated from the known lesion region and the chosen background regions in the reconstructed images using different CT maps:

$$\mathrm{TBR} = \frac{\mathrm{Mean}_{\mathrm{hot\ lesion}}}{\mathrm{Mean}_{\mathrm{background}}} \tag{4.3}$$

(iv) Contrast and noise

In the noise-free reconstructed images, we measured the average voxel value of the lesion as $\mathrm{A}_{\mathrm{lesion}}$ and average voxel value of a ROI drawn in the lung as $\mathrm{A}_{\mathrm{lung}}$. The lesion contrast was defined as

$$\mathrm{Contrast} = \frac{\mathrm{A}_{\mathrm{lesion}} - \mathrm{A}_{\mathrm{lung}}}{\mathrm{A}_{\mathrm{lesion}} + \mathrm{A}_{\mathrm{lung}}} \tag{4.4}$$

The noise level was measured by the normalized standard deviation (NSD) of the voxels in an approximately uniform ROI within the mid-lung region with a total number of 78 voxels. The NSD was calculated by dividing the SD of the ROI by the ROI mean, where m is the number of voxels in the ROI, μ is the mean voxel value of the ROI, x is the voxel count value in the noisy reconstructed images, and j is the voxel index.

(4.5)

$$NSD = \frac{SD}{mean} = \frac{\sqrt{\frac{1}{m-1}\sum_{j=1}^{m}(x_j - \mu)^2}}{\mu}$$

(e) Image profile

A vertical profile was drawn across the lesion and the adjacent diaphragm area to indicate the potential lesion detectability (Figure 4.3B).

4.2 RESULTS

From visual assessment, the IACTs modeled the respiratory motions similarly to the CACT (Figure 4.3A). The reconstructed PET images with AC using CACT and IACT showed no significant artifacts as compared to the original phantom (Figure 4.2A, 4.3B & 4.4). Significant artifacts were observed in the PET reconstructed images using HCTs for AC in both noise-free and noisy data (Figure 4.3D & 4.4). The lesion volume and uptake was more prominent for PET reconstructed images using HCT-8 for AC, though artifacts were still observed near the diaphragm region. For $IACT_{2o}$, the lesion movement can be modeled exactly for motion amplitude of 2 and 3 cm but not for 4 cm (Figure 4.5A). OFM fails to model the 4cm lesion movement with $IACT_{2o}$ while B-spline can model this motion (Figure 4.5B).

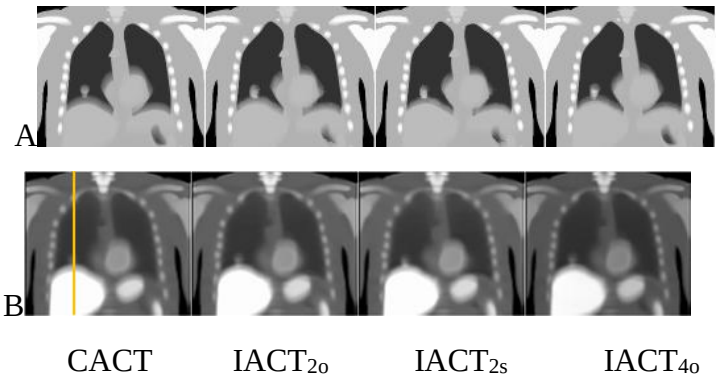

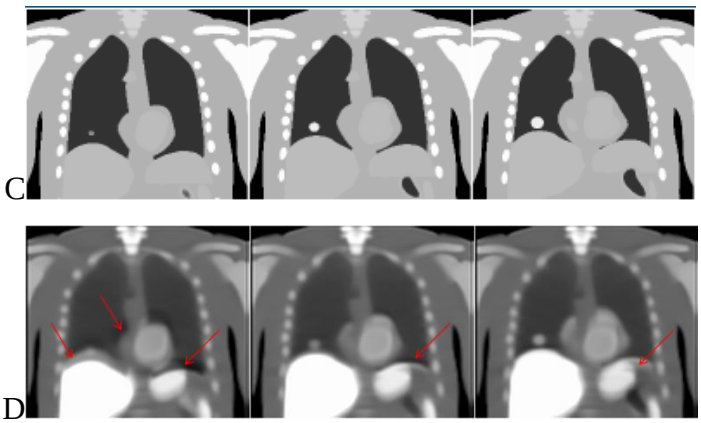

Figure 4.3 (A) & (C) Different attenuation maps for AC and their corresponding noise-free PET reconstructed images (B) & (D) for respiratory motion = 2 cm. Significant misalignment artifacts were observed for the PET images using HCTs for AC (red arrows).

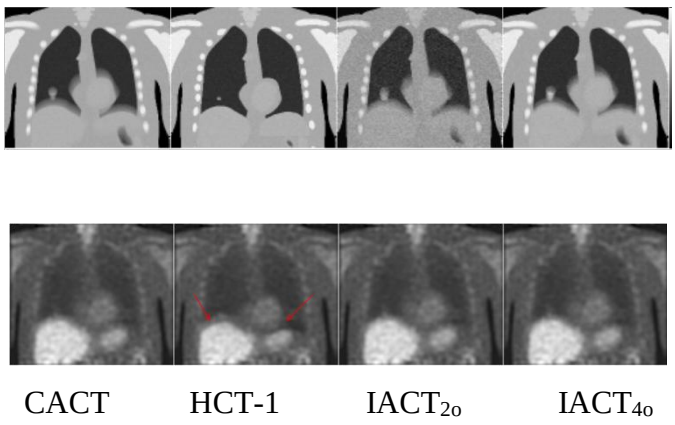

Figure 4.4 Top row: different noisy attenuation maps for AC. Bottom row: their corresponding noisy PET reconstructed images generated from noisy sinogram with 100 updates and Butterworth filtering with cutoff frequency of 0.21 $pixel^{-1}$ for maximum respiratory motion of 2 cm. Significant misalignment artifacts were observed for the PET images using HCTs for AC (red arrows).

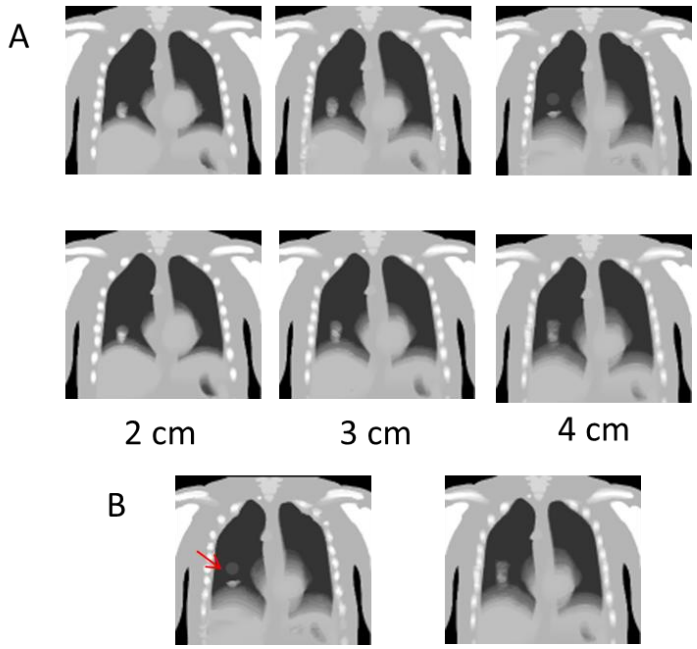

Figure 4.5 (A) Top row: $IACT_{2o}$ and bottom row: $IACT_{4o}$ maps for 3 different motion amplitudes. (B) Left: OFM fails to model the 4cm lesion movement with $IACT_{2o,}$ Right: B-spline can model this motion.

The quantitative NMSE and MI showed that HCT-1 and HCT-8 had the worst performances for motion amplitudes of 2 cm (Figure 4.6, 4.7). As expected, reconstructed images using AC with CACT had least difference as compared to the original phantom, following by $IACT_{4o,}$ $IACT_{2o,}$ $IACT_{2s}$ and HCT-5. Our results showed that $IACT_{2o}$ provided similar accuracy as compared to $IACT_{4o}$ and even CACT, with MI difference of <0.41% and <2.17% respectively, reassuring our findings in the previous clinical studies [63]. With a slight misplacement of these two phases, the resultant $IACT_{2s}$ still showed comparable accuracy to $IACT_{2o}$ with MI difference of <2.23%.

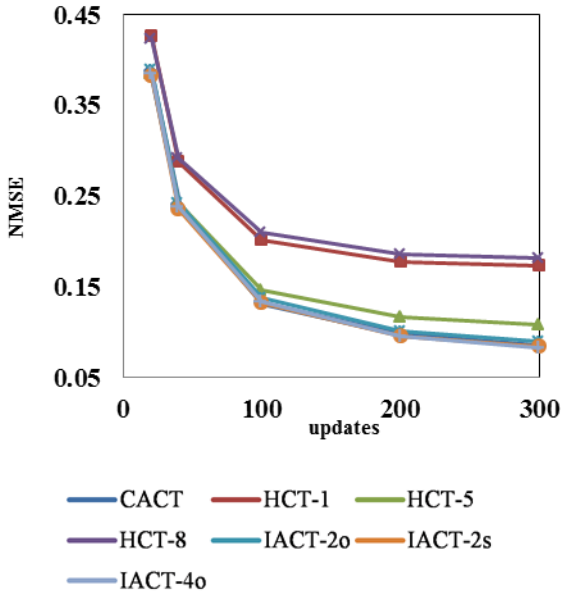

Figure 4.6 Noise-free results of NMSE for respiratory motion of 2 cm.

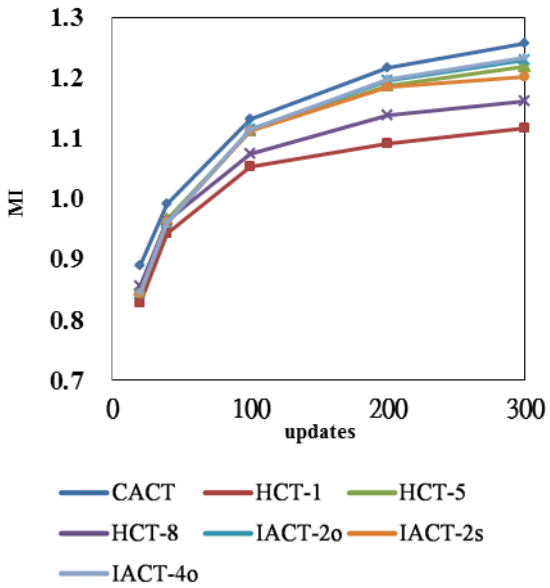

Figure 4.7 Noise-free results of MI for respiratory motion of 2 cm.

For the TBR results of the noise-free simulation, AC with HCT-1 showed inferior results as compared to others (Figure 4.8), as also indicated by visual assessment (Figure 4.3D). IACTs performed similarly as compared with CACT for AC in terms of TBR (Figure 4.8), while HCT-8 showed higher TBR as compared to others. Image profile results were also accordant with visual assessment that HCT-8

and HCT-5 provided better lesion detectability as compared to others but they caused artifactual increase of diaphragmatic uptake near the liver (Figure 4.9). A summary of the noise-free results for motion amplitude of 2 cm, 3 cm and 4 cm of 300 updates was shown in Table 4.1.

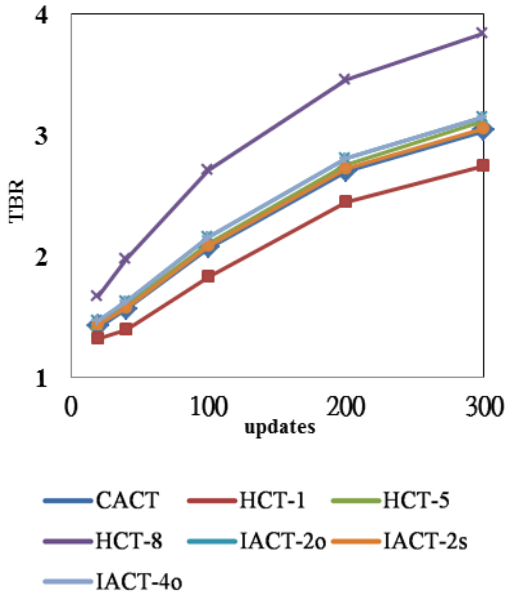

Figure 4.8 Noise-free results of TBR for respiratory motion of 2 cm.

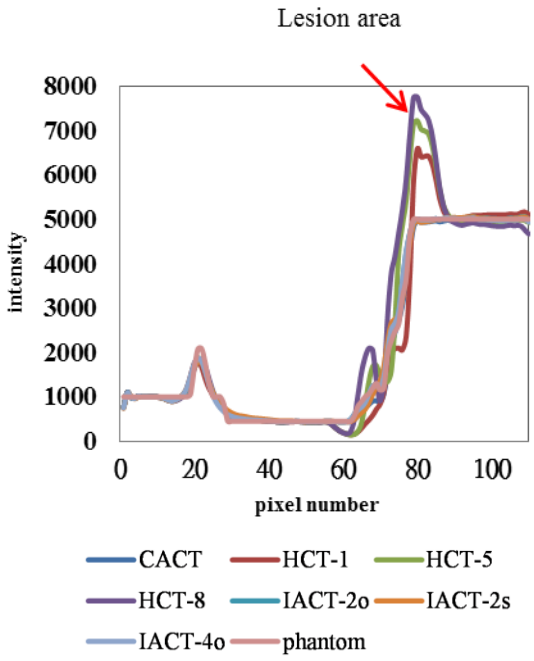

Figure 4.9 Noise-free results of image profiles for respiratory motion of 2 cm.

Noisy simulations (Figure 4.10, 4.11) had accordant NMSE and MI results with the noise-free simulation (Figure 4.6, 4.7). Dotted lines (IACT-2o_noise) are the results for noisy $IACT_{2o}$ that generated from 2 noisy CT phases. Figure 4.12 showed the relationship between lesion contrast and NSD for different AC schemes in the noisy simulation. The points on the curves represented number of updates, increasing from the left to the right side for OS-EM algorithm. The bottom right region indicated better image quality, i.e., lower noise and higher contrast. The HCT-1 clearly showed inferior noise-contrast trade-off among the 4 curves.

Table 4.1 Summary of the noise-free results of different CT AC methods at 300 updates.

Motion amplitude	indices	CACT	HCT-1	HCT-5	HCT-8	IACT-2o	IACT-2s	IACT-4o
2 cm	NMSE	0.085	0.140	0.094	0.139	0.088	0.086	0.093
	MI	1.256	1.118	1.218	1.161	1.229	1.234	1.201
	TBR	3.040	2.748	3.118	3.838	3.149	3.149	3.051
3 cm	NMSE	0.084	0.173	0.108	0.182	0.089	0.083	0.084
	MI	1.218	1.036	1.160	1.086	1.176	1.210	1.193
	TBR	2.477	2.427	2.410	3.439	2.622	2.513	2.495
4 cm	NMSE	0.078	0.204	0.120	0.222	0.090	0.082	0.089
	MI	1.324	1.085	1.228	1.153	1.247	1.303	1.241
	TBR	2.089	2.094	1.955	2.988	1.851	2.055	1.708

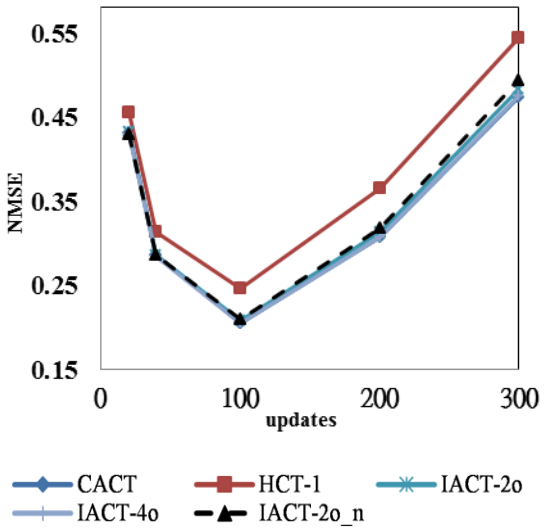

Figure 4.10 Noisy results of NMSE for respiratory motion of 2 cm

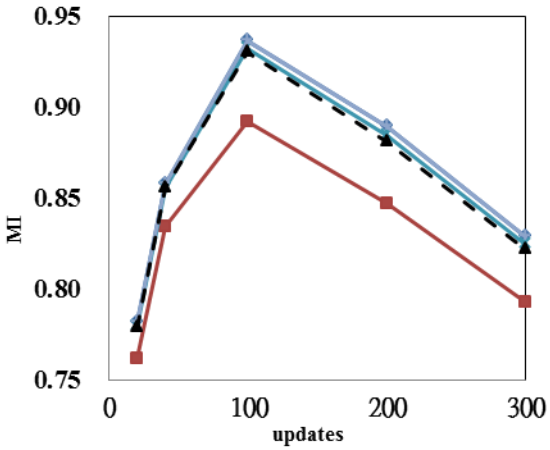

Figure 4.11 Noisy results of MI for respiratory motion of 2 cm.

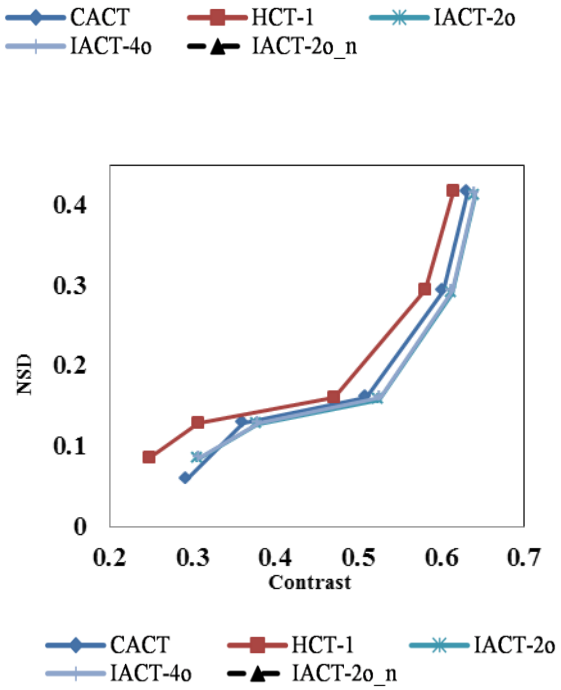

Figure 4.12 Image noise level as a function of lesion contrast for different AC schemes for respiratory motion of 2 cm

4.3 DISCUSSION

For the general global measurement of image quality indices such as NMSE and MI (Figure 4.6, 4.7, Table 4.1), HCT-5 showed the best performance among HCTs in this study. It matched with our prediction that mid-phase breath-hold HCT was more similar to CACT. However, HCT-5 still worked slightly inferior to the IACTs quantitatively as shown in the previous results. Also, it is difficult to assure that the HCT-5 (mid-phase of the respiratory cycle) would be captured for the clinical CT acquisition, as it is difficult for patients to hold their breath during the mid-respiratory phases.

On the other hand, for the indices more related to lesion detection such as TBR and image profile, HCT-8/HCT-5 showed even better performance as compared to CACT for AC (Figure 4.8, 4.9). This is probably caused by the fact that HCT-8 coincidently captured the lesion with its full size in this case, while HCT-8 for AC may fail to detect the lesions located at other regions of the thorax.

Moreover, noise-contrast trade-off has been validated, and HCT-1 showed the worst lesion detectability in all detection related indices, matched with the visual assessment that the diaphragm mismatch artifacts blurred out the lesion and caused the uptake underestimation.

4.3.1 NOISY CT SIMULATION

Generating IACTs using noisy CT phases would be a more realistic representation for the clinical data with higher noise and lower radiation dose. In order to reduce data redundancy, we just simulated the noise based on the clinical data for CACT, HCT-1, $IACT_{2o}$ and $IACT_{4o}$ (Figure 4.4). One can infer HCT-5 and HCT-8 should have the similar noise level as compared to HCT-1, and $IACT_{2s}$ should have the similar noise level as compared to $IACT_{2o}$ in the noisy CT simulations. The noisy simulation results for a motion of 3 cm were accordant with those of the motion of 2 cm and were not shown here. To evaluate the noise effects in the noisy simulation, we compared the noisy IACTs generated by noisy respiratory phases (IACT-2o_noise) and noise-free phases (IACT-2o), i.e., noise modeled on the resultant IACT based on the clinical

IACT data. Their similar quantitative results indicated that the noise level on a realistic single CT phase did not significantly affect the OFM calculation in this study (Figure 4.10, 4.11).

4.3.2 LESION SIZE AND OTHER EFFECTS

We simulated a 25 mm-diameter spherical lesion with all 3 different motion amplitudes in this study. Pevsner *et al.* showed that the underestimation of the activity concentration in the sphere phantoms can reach 75% for the standard clinical protocol, depending on the spherical sizes [72]. Hamill *et al*. showed that quantitation of smaller lesions were more affected by the respiratory motion blurring. i.e., 20 mm tumors was still feasible for conventional PET/CT protocol when the motion is less than 15 mm, while 10 mm tumors were more significantly blurred and their SUV values were more underestimated than those of the 20 mm tumors [39]. Our results showed that the IACT method works for a 25 mm lesion for motion amplitude of ~ 3 cm using the OFM.

4.3.3 FURTHER CONCERN FOR THE CLINICAL STUDY

A clinical study with ~100 patients showed that ~90% of the clinical patients had $\leqq$3 cm respiratory motion amplitude and ~95% of patients had $\leqq$4 cm motion [25], indicating the IACT method should work well for most of the patients. Our results showed that, the lesion movement cannot be modeled exactly for $IACT_{2o}$ in motion = 4 cm while IACT method using 4 original phases ($IACT_{4o}$) worked well for maximum breathing motion amplitude of 4 cm (Figure 4.5). However, we found that the lesion movement for motion amplitude of 4 cm can still be modeled correctly by B-spline for $IACT_{2o}$ (Figure 4.13). Hence we chose the B-spline method in the following clinical study. Besides, slight time errors may exist for capturing these two extreme phases in the real clinical situations. However, our results of $IACT_{2s}$, i.e., with "shifted" end-inspiration and end-expiration phases for interpolation, were very similar to $IACT_{2o}$, indicating the robustness of this method.

On the other hand, generating the IACT using just the end-expiration and end–inspiration phases would have the minimal dose. It may also be feasible to achieve the same dose reduction of using only two original phases for interpolation with improved image quality by using more phases for interpolation and reducing the dose for each phase at the same time. However, capturing multiple phases during a respiratory cycle may not be feasible in clinical practice with the considerations of x-ray beam on/off delay and patients' compliance.

Another concern is that the extreme phases used for IACT cannot be obtained via patients' voluntary breath-holding, as they would be very different from the free-breathing state as in the PET and would generate respiratory artifacts. Thus, the clinical realization of the IACT technique highly relies on the implementation of the active breathing control (ABC) device to ensure the captured respiratory phases represent a free-breathing state of the patients [73]. An associated hardware and acquisition software have been developed for a clinical PET/CT study and will be discussed in the next Chapter.

CHAPTER 5 : CLINICAL STUDY

In this chapter, we aim to realize the clinical implementation of IACT with the aid of an active breathing controller (ABC) prototype [74], and investigate its potential improvement for AC as compared to the conventional HCT in patients with thoracic lesions.

5.1 ACTIVE BREATHING CONTROLLER (ABC)

Voluntary breath-holds of end-expiration and end-inspiration phases performed by the patients themselves could probably not represent the normal breathing state as in the PET acquisition. Using these phases to generate IACT may introduce even more artifacts as compared to conventional HCT. Thus, to capture two breath-hold CT scans at normal end-inspiration and end-expiration phases, an ABC system (Figure 5.1 A&B) was developed in this study based on the design originally proposed for radiotherapy [73].

A

B

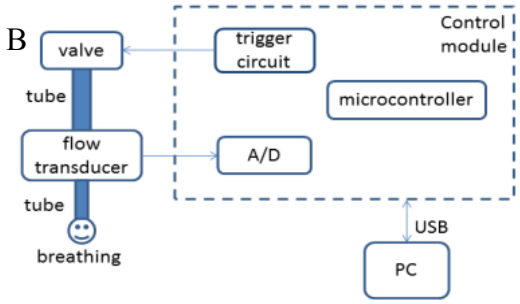

Figure 5.1 (A) Overview and (B) block diagram of the ABC system

5.1.1 WORKING PRINCIPLE

This non-invasive device integrates a spirometer, an air mask and a tube-valve system that are controlled by a PC. The flow sensor detects real-time breathing flow rate of the patients and samples the signal to the microcontroller. The microcontroller preprocesses the signal and sends it to the PC through a USB connector. A program based on C++ has been developed to process the input signal and control the switching of the valve. It can automatically detect the change of the air flow direction to locate the end-inspiration and end-expiration phases. The flow can be integrated to determine the lung volume change during the respiratory cycle. The system is generally composed two different modules: signal acquisition module and valve control module.

(i) Signal Acquisition Module

We chose the Microbridge's MB-LP low pressure sensor (Figure 5.2A) as the micro-flow sensor. This model senses the differential air pressure from the gas flow (nL/s) through an integrated air-flow channel having high pneumatic impedance (flow-impedance). The transducer is a Microelectromechanical system (MEMS)-based thermal-anemometer embedded on a monolithic silicon chip. Rejustor technology combined with the complementary metal-oxide-semiconductor (CMOS) circuitry provides on-chip integrated analog-only electronics for temperature compensation and voltage-resistor conditioning.

Pitot tubes (Fig 5.2B) are traditionally used as open-air measurement probes for air speed. The signal acquisition module uses the Pitot tube probes with the sensor for effective air speed measurement.

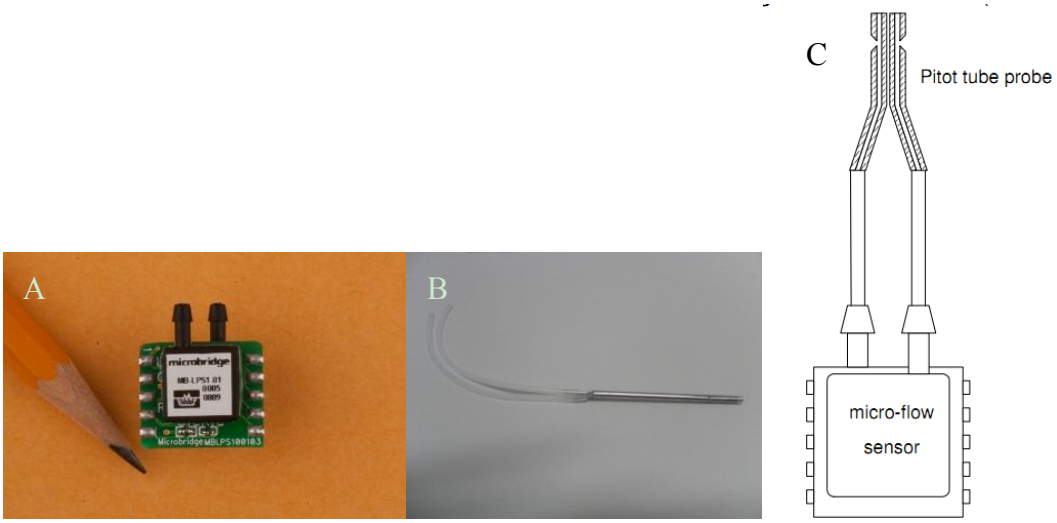

Figure 5.2 Integration of the flow sensor and pitot tube: (A) flow sensor; (B) pitot tube; (C) integration of A and B.

To characterize the sensor, a simple experimental setup was assembled (Figure 5.3). A mask is connected with a tube to acquire the patient's breathing signal. The Arduino Uno microcontroller reads the signal from the sensor output pin. The serial to USB port on the input-output (IO) board sends the signal to PC.

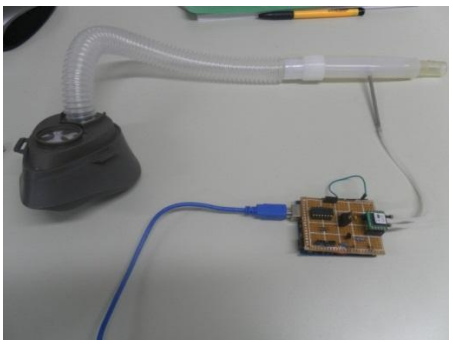

Figure 5.3 The assembly of the signal acquisition setup

A program based on C++ was written in Integrated Development Environment IDE Qt (Digia, Finland) is designed to process and display the read-in signal. The

interface is shown in (Figure 5.4A). The operator can setup all the parameters: serial port number, offset due to the environment change and valve closing time. The signal acquisition design can be separated into 3 parts (Figure 5.4B):

(a) Serial port selection. It contains three files to support: com.ui, com.h, com.cpp. Its function is to select available serial port number (COM) on the PC.

(b) Main window that includes the key functions. It contains other three files to support: dialog.ui, dialog.h, dialog.cpp. Its functions are: initializing the selected port in the first part; initializing the main plots of flow and volume in the virtual oscilloscope; reading in the signal from the IO board; updating the plots of flow and volume in the virtual oscilloscope; recording elapsed time and valve status change time by Timers; signal processing from the read-in signal; providing algorithm to calculate the valve close time.

(c) Data output. It contains two files to support: io.h, io.cpp. Its function is to save the flow, volume signals and experiment status into output files.

A

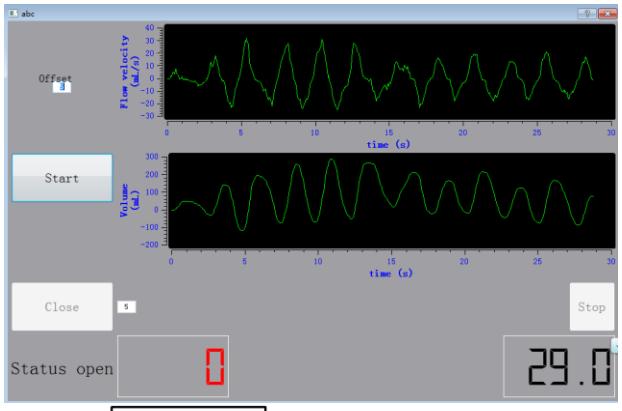

B

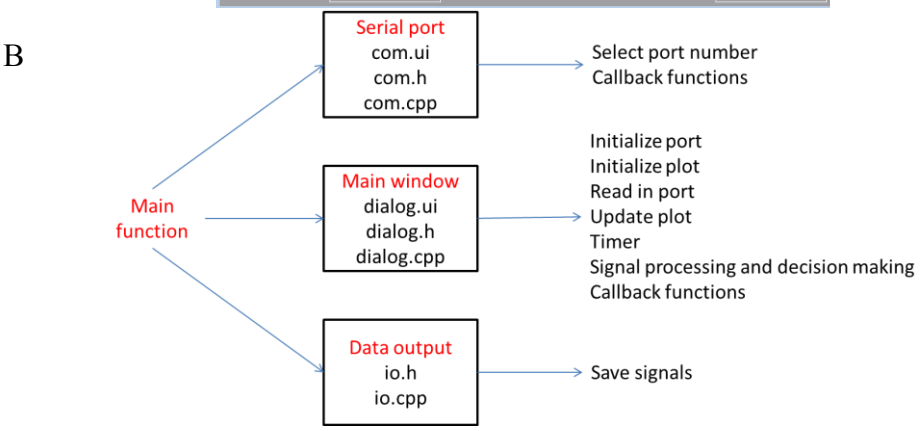

Figure 5.4 (A) User interface and (B) design diagram

(ii) Valve control module

The signal acquisition module can detect the change of the air flow direction which indicates the end-inspiration and end-expiration phases of breathing. In the following clinical study, the operator needs to start the CT scan manually once the patient is forced to hold their breaths by the ABC during the end-expiration and end-inspiration phases. When the valve which is attached to the end of the tube closes, the patient's breath can be held at a certain breathing state. An opened solenoid valve (Figure 5.5A) with 16 mm inner diameter is used to control the air flow. It has rated power of 2 W and voltage of DC 12 V.

Figure 5.5 Assembled valve control module: (A) opened solenoid valve and (B) assembled valve control module

Figure 5.6 is the diagram of the control circuit module. V1 is the supply power source of the valve; R1 is the valve which has a 20 K internal resistance; D1 is a Schottky Diode, 1N5819; M1 is a N-Channel Power MOSFET, IRF510; Q1 is a NPN General Purpose Amplifier, 2N3904; A1 is one channel of a hex inverter, 74HC04D; V2 is the output voltage level from the microcontroller board's output pin and SW is a voltage control switch controlled by high or low level input voltage; R2, R3, R4, R5 are all the resistors. PC will send the valve closing and opening signal through the USB connector after the operator signals on the program interface.

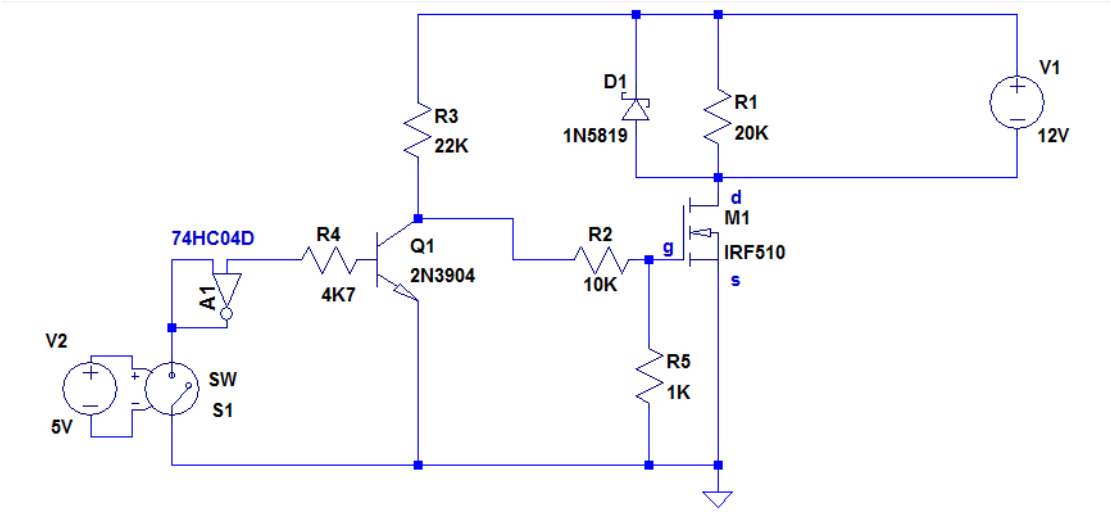

Figure 5.6 Control circuit module diagram.

The circuit has two operating modes to make the valve closes and opens respectively. The default status of the valve is open. In this status, input is low level voltage L and SW is open. The inverter inverts the voltage to high level H, and the NPN transistor will invert the gate voltage back to low level L again. So N-MOSFET will work in the "cut-off" region or "OFF mode". The transistor acts like an open circuit and there will be no current flows through the channel, hence there is no current that flows through the valve either. Then the valve will stay at the constant open status (default).

To let the valve to be closed, V2 has to be a high level voltage H and then SW is closed. The inverter inverts the voltage to low level L. The NPN has two functions here: 1. invert the voltage to high level H again; and 2. amplify the gate current from the output pin (~20 mA) to a level that can drive the MOSFET to work in the "saturation region" or "ON mode". The resistance of the drain-source channel changes from many hundreds of kΩ to less than 1 Ω, effectively an open circuit. The valve will stay at the closed status.

Once the preset valve closing time has elapsed, the program will automatically send a signal to enable the high input voltage level H to let SW open again. The valve will return to the default status and open again.

5.1.2 ACQUISITION PROCEDURE

Before the acquisition, a system calibration is performed in order to compensate the signal drift caused by the substantial change of temperature and atmospheric pressure. Subjects are coached before the actual CT scans to adapt to the ABC. ABC device samples the respiratory signal by detecting the air flow with 20 Hz sampling frequency, while the peaks and the valleys of the signal indicate end-inspiration and end-expiration phases respectively. During the acquisition, the operator observes the real time signal, indicates when he/she is ready to acquire the CT data. The acquisition program then automatically detects the next extreme phase and sends a high level voltage signal to the electronic board to close the valve connected to the breathing tube with <0.1 s. The operator then manually starts the HCT scans once the patient is controlled to hold their breath for ~6 s during each extreme phase. The flow rate signals could be integrated to determine the change of lung volume during the respiratory cycle. Sample lung volume changes during the breathing cycles under the ABC control are shown in Figure 5.7. The change of the lung volume of a volunteer while his breath-hold was actively suspended by the ABC. Red arrows indicate the closing period of the valve.

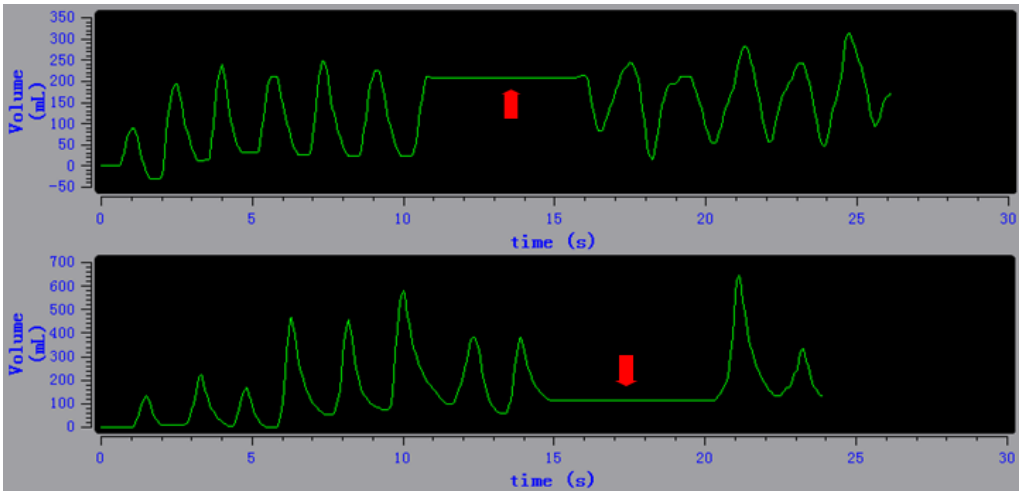

Figure 5.7 A volunteer's lung volume changed during the end-inspiration and end-expiration breath-hold controlled by ABC

5.2 METHODS AND MATERIALS

5.2.1 PATIENT POPULATION

Between October 2012 and December 2012, we recruited 15 patients with a total of 18 lesions in different thoracic regions: left upper lobe (2), right upper lobe (4), right hilum (3), right lower lobe (3), left hilum (2) and esophagus (4). A summary of their demographic data is shown in Table 5.1. This study was conducted in the Taipei Veterans General Hospital and was approved by its Institutional Review Board. Written informed consents were obtained from all patients. All patients were recruited through their scheduled whole-body PET/CT procedures, and those who were with history of inferior pulmonary function or were unable to follow the breath-hold procedures were excluded from this study (n = 3).

Table 5.1 Patients demographic data.

Patient no.	Sex	Age (yr)	Lesion location	Lesion volume (c.c.)
1	F	65	Left upper lobe	5.29
2	F	66	Right upper lobe	8.28
3	M	86	Right middle lobe, close to rib	3.45
4	M	81	Right middle lobe	21.64
5	M	59	Left upper lobe	7.63
6	M	51	Right upper lobe	2.15
			Right lower lobe	4.54
			Left upper lobe, close to rib	1.3
7	M	59	Right middle lobe	1.45
			Left hilum	5.56
8	M	66	Right hilum	1.6
9	M	72	Right upper lobe	7.09
10	M	88	Right upper lobe, close to rib	9.53
11	M	68	Right middle lobe	11.39
12	M	61	Esophagus	29.6
13	M	47	Esophagus	25.38

14	M	42	Esophagus	4.79
15	M	60	Esophagus	15.48

5.2.2 ACQUISITION PROTOCOL

Patients were injected with 300-480 MBq of ^{18}F-FDG according to each patient's weight, and scanned 1 hr post injection. For each patient, four imaging sessions were acquired:

(i) standard shallow free breathing whole-body HCT (120 kV, smart mA (range 30–150 mA), helical mode, 0.984:1 pitch, 0.5 s gantry rotation);

(ii) whole-body PET for 7 bed positions with 3 mins/bed;

(iii) end-inspiration and end-expiration breath-hold HCTs aided with ABC for the thoracic region (120 kV, 10 mA helical mode, 0.984:1 pitch, 0.5 s gantry rotation time and a total of 4.4 s/scan);

(iv) thoracic PET for 2 bed positions with 3 mins/bed.

All scans were acquired using a GE STE PET/CT scanner in 3D mode. The thoracic PET was performed due to the fact that the patients changed position after the whole body session for accommodating the ABC device.

5.2.3 IACT GENERATION

As discussed in the previous part, B-spline, a deformable image registration algorithm, was applied to calculate the deformation vectors which includes lateral, anterior-posterior and inferior-superior displacement for each voxel on two CT volumes, i.e., end-inspiration and end-expiration phases obtained from ABC, based on the ITK [75]. One CT image was chosen as the fixed image, i.e., end-inspiration phase, while the other was used as the moving image, i.e., end-expiration phase.

For the computational efficiency, two sub-steps with boost techniques were applied in the real implementation (Figure 5.8). A single rigid registration was conducted in the first step. Three stages of B-spline registration were performed later using a multi-resolution method in the second step. The grid resolution of the control points improved and their grid-spacing decreased along different stages in this step. The deformation field was determined when the mean square error of the two CT images was smaller than a positive value ϵ (0.001) in each resolution level.

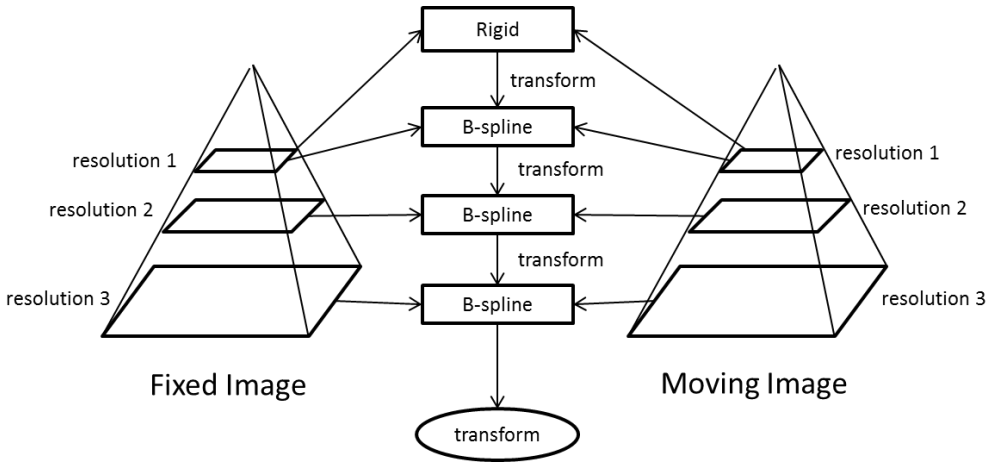

Figure 5.8 Multi-resolution approach estimates the final transform between fixed image and moving image

The forward deformation vector ϕ_{ie} was calculated from end-inspiration phase #1 to end-expiration phase #7 and the backward deformation vector ϕ_{ei} was calculated from phase #7 to phase #1. For interpolation of $\phi_{ie}$and ϕ_{ei} to obtain the interpolated phases, a diaphragmatic movement function during respiratory cycles was introduced [69]:

$$z(t) = z_0 - bcos^{2n}\left(\frac{\pi t}{\tau}\right) \qquad (5.1)$$

where *z(t)* = position of diaphragm at time *t*, z_0 = diaphragm position at end-expiration, b = amplitude of motion, τ = period of motion, and n = degree of asymmetry which depends on the patient-specific respiratory signals. The power of "2n" made Equation 5.1 resulted in more phases near the end-expiration than near the end-inspiration. The inspiration/expiration ratios were calculated for one respiratory

cycle for different integer n from Equation 5.1 and compared with the actual ratios measured in the acquired breathing signal from each patient, and n was determined when its corresponding ratios had the best fit with the measured data. In our study, n=3 was used for most patients except n=2 for patient#7 and n=4 for patient#12. To generate intermediate images, ϕ_{ie} was divided based on *z(t)* to obtain interpolated deformation fields. Thus, we can generate interpolated phases #2, #3, #4, #5, #6 by warping original phase #1 based on ϕ_{ie} (Figure 5.9). Similarly, phases #8, #9, #10, #11 and #12 were warped from phase #7 based on ϕ_{ei}. The final IACT was generated by averaging the image intensity of 10 interpolated and 2 original extreme phases, i.e., a total of 12 phases.

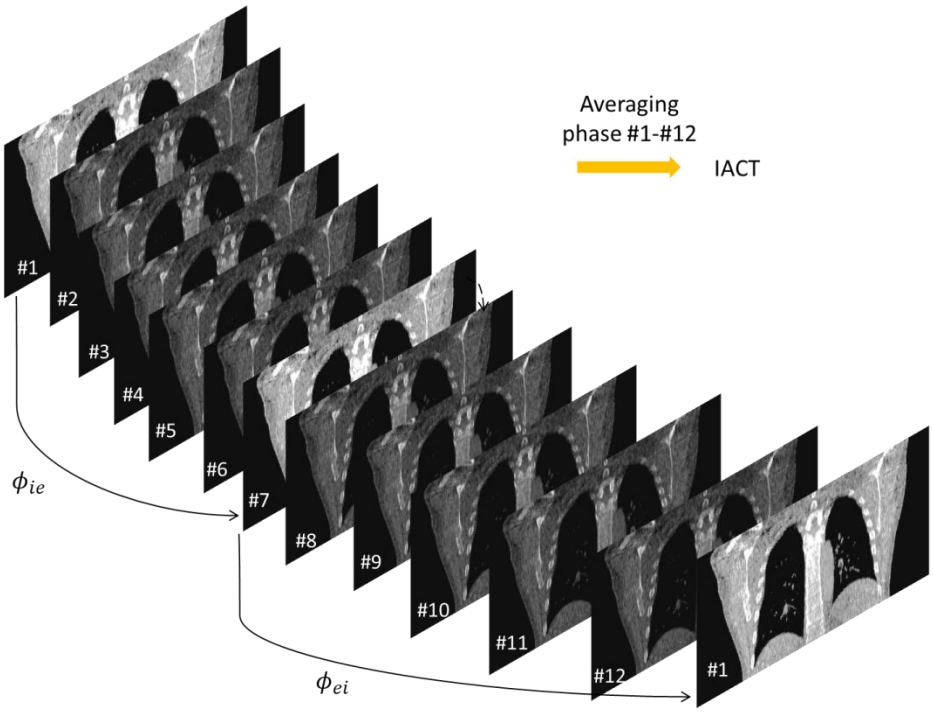

Figure 5.9 The deformation fields obtained from B-spline method were used to generate the interpolated images for IACT based on a semi-patient specific sinusoidal function

5.2.4 Data post-processing and image analysis

The PET raw data were reconstructed using 3D OS-EM (28 subsets; 2 iterations; pixel matrix of 128×128) algorithm available on the PET/CT workstation. The PET

sinograms were corrected for random, scatter, isotope decay and attenuation using HCT and IACT respectively. The PET reconstructed images with AC using HCT and IACT, i.e., PET_{HCT} and PET_{IACT}, were registered with associate CT for further analysis.

(i) Misalignments between PET and CT

A 3D volume-of-interest (VOI) was delineated for each lesion on PET images using a semi-automatic region growing method with a 50% cut off threshold of the maximum intensity value [76-78]. The corresponding delineation for VOI in the CT images was performed with the "lung" window by a radiation oncologist. The coordinates of the centroid of the lesion in PET_{HCT}, HCT, PET_{IACT} and IACT were determined on the chosen VOIs [40, 79]. The distances (*d*) between the lesion centroid of PET and associate CT were then obtained.

(ii) SUV

For each lesion, maximum SUV value (SUV_{max}) and mean SUV value (SUV_{mean}) were measured based on the VOIs drawn on the PET_{HCT} and PET_{IACT} images.

(iii) Radiation dose

For different CT protocols and subjects, the radiation dose was expressed using the effective dose in mSv for the thoracic region. An approximation of the effective dose was obtained by multiplying the volume CT dose length product (mGy-cm) as reported by the manufacturer's software with a conversion factor k (0.014 mSv mGy-1 cm-1) [80].

5.3 RESULTS

For all 15 patients with 18 lesions, IACT generally reduced lesion mismatch (*d*) between CT and corresponding PET attenuation corrected images (Table 5.2), with average decrease of 1.34 ± 1.79 mm among all measurable lesions. The centroid difference was not obtainable for patients with esophageal lesions as they could not be delineated on the CT images.

Meanwhile, the SUV_{max} and SUV_{mean} for the lesions are summarized in Table 5.2. PET_{IACT} generally showed increased SUV_{max} and SUV_{mean} for all lesions when

compared to PET_{HCT}. The percentage increments (%diff) are 30.95 ±18.63% and 22.39 ±15.91% for SUV_{max} and SUV_{mean} respectively.

Table 5.2 Summary of different quantitative figures-of-merit for HCT and IACT AC methods

Patient no.	**SUV_{max}**			**SUV_{mean}**			***d* (mm)**		
	PET_{HCT}	PET_{IACT}	%diff	PET_{HCT}	PET_{IACT}	%diff	HCT/ PET_{HCT}	IACT/ PET_{IACT}	diff. (mm)
1	5.98	7.01	17.22	2.48	2.78	12.1	6.28	5.91	-0.37
2	7.99	9.07	13.52	3.89	5.81	49.36	3.79	6.49	2.7
3	4.64	6.26	33.84	2.89	2.98	3.11	6.6	4.67	-1.93
4	12.03	14.97	24.44	4.96	5.75	15.93	4.68	4.59	-0.09
5	3.27	5.67	73.39	1.23	1.8	46.34	7.32	6.22	-1.1
6	6.39	7.91	23.79	3.77	4.83	28.12	4.74	1.97	-2.77
	2.47	2.67	8.1	1.32	1.52	15.15	6.58	4.47	-2.11
	3.5	4.35	24.29	2.22	2.77	24.77	13.77	8.79	-4.98
7	1.98	2.77	39.9	1.2	1.91	59.17	5.27	4.39	-0.88
	2.69	3.29	20.07	1.51	1.53	1.32	12.12	14.67	2.55
8	1.53	2.35	53.59	1.01	1.11	9.9	6.55	6.47	-0.08
9	7.84	8.46	7.91	3.96	4.57	15.4	2.93	0.57	-2.36
10	1.84	2.83	53.8	1.47	1.92	30.61	4.91	5.53	0.62
11	7.65	10.71	40	5.32	6.75	26.88	9.34	1.36	-7.98
12	15.77	21.3	35.07	9.3	11.75	26.34			
13	4.77	4.98	4.4	3.23	3.66	15.48	N/A		
14	8.12	10.85	33.62	5.21	5.77	10.75	(Lesions cannot be delineated on CT images)		
15	6.27	9.41	50.08	3.69	4.14	12.2			
Mean	5.82	7.49	30.95	3.26	3.96	22.39	6.78	5.44	-1.34
SD	1.94	2.21	18.63	1.45	1.62	15.91	3.07	3.46	2.79

Sample images of 3 patients with thoracic lesions are shown in Figure 5.10, Figure 5.11 and Figure 5.12 respectively. In Figure 5.10, the IACT AC method provided a better matching for the CT and PET image as compared to HCT for AC. The visual assessment matched with the quantitative measurement of the centroid difference between CT and PET in Table 5.2 ($d_{HCT/PET_{HCT}}$ =9.34 mm; $d_{IACT/PET_{IACT}}$=1.36 mm; diff=-7.98 mm).

For another patient as demonstrated in Figure 5.11, the contrast of the lesion in the right upper lobe substantially improved for PET_{IACT} as compared to $PET_{HCT,}$ with increase of SUV_{max} and SUV_{mean} of 53.8% and 30.61% respectively. The general resolution also improved for PET_{IACT} as compared to PET_{HCT} in this patient as indicated in the vertical profiles drawn on Figure 5.11C, where the lesion full-width-at-half-maximum appeared to be smaller with improved structure details in the liver region on PET_{IACT}. The PET_{HCT} had severe "cold" artifacts around the left ventricle region and also in the region close to the left diaphragm, while the artifacts reduced in the PET_{IACT}. Signature curvilinear artifact was also observed on PET_{HCT} in patient#13 with esophageal cancer (Figure 5.12).

The estimated effective dose was 0.38 mSv for IACT for the thoracic region, while HCT had an average effective dose of 2.1 mSv (1.58-2.42 mSv) in the same region. The IACT reduced up to 84.29% effective dose as compared to HCT method in this study.

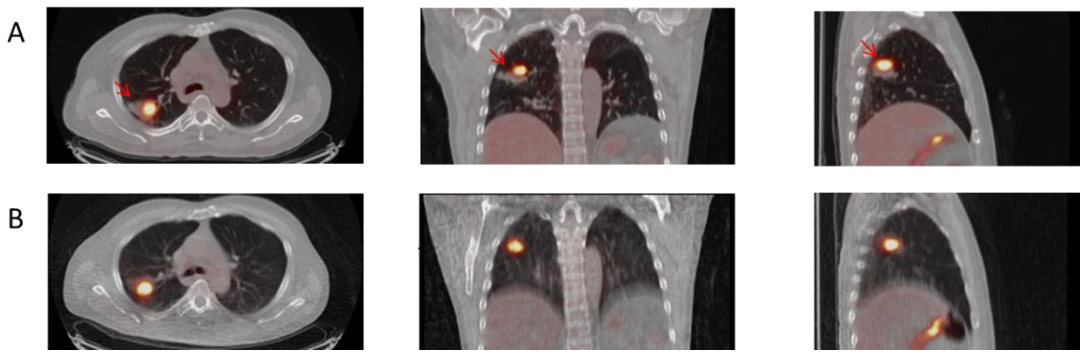

Figure 5.10 Transaxial (left), coronal (middle), and sagittal (right) views of the fused PET/CT images for (A) HCT- and (B) IACT-AC for patient #11. Red arrows indicated a lesion in the right upper lobe of the lung.

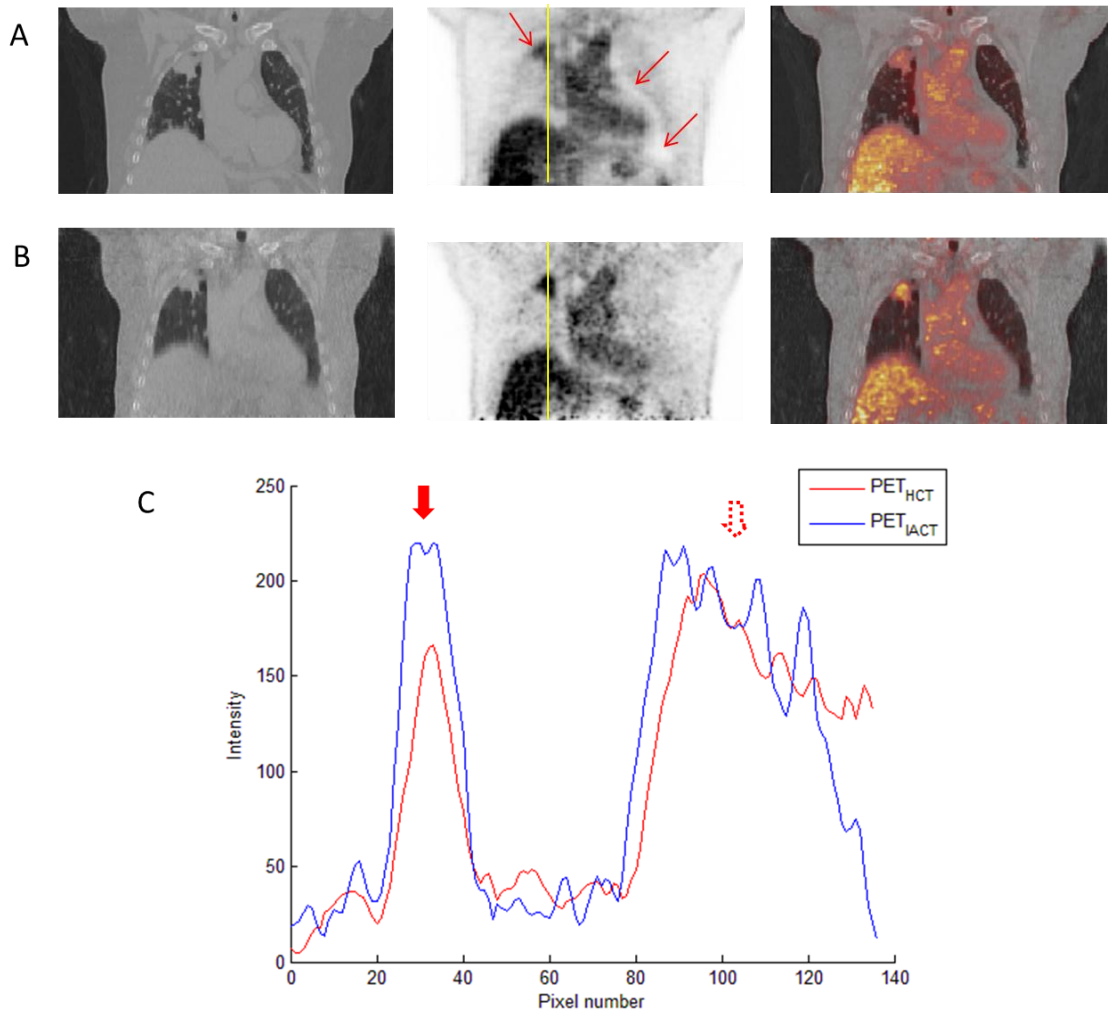

Figure 5.11 Sample coronal images of (A) HCT (left); PET_{HCT} (middle); fusion image (right) and (B) IACT (left); PET_{IACT} (middle); fusion image (right) for patient #10. Artifacts around the left diaphragm and left ventricle region were observed on the PET_{HCT} images (red arrows). (C) Vertical image profiles drawn across the lesion on PET_{HCT} and PET_{IACT} images. Red arrow indicated the lesion area and the dotted red arrow indicated the liver region.

Figure 5.12 Coronal views of (A) PET_{HCT} and (B) PET_{IACT} for patient #13. Curvilinear artifact was observed on PET_{HCT} (red arrow) but reduced on PET_{IACT}.

5.4 DISCUSSION

5.4.1 ABC FEASIBILITY AND STABILITY

Right before the CT scan, each patient will hear a sharp sound from the closing valve and a backward force from the tube will then enforce the patient to hold his/her breath. The time from the valve closing to patient's response lasts <1 s. We thus set the valve closing time to ~6 s to enable patients to hold their breath sufficiently long enough for the HCT scan, which usually takes 4.4 s. The short breath-hold time particularly enhances the feasibility of this study, as compared with other breathing-instruction methods [40]. For the stability, our former simulation study showed that the IACT generated from the "shifted" respiratory phases, i.e., the phases right after the extreme phases, provided very similar results to the IACT generated from the exact end-inspiration and end-expiration phases. However, some patients may have residual breathing after the valve is closed (Figure 5.13). Thus, after coaching, all patients underwent a mock acquisition before the experiment to confirm their compliance of breath-holding.

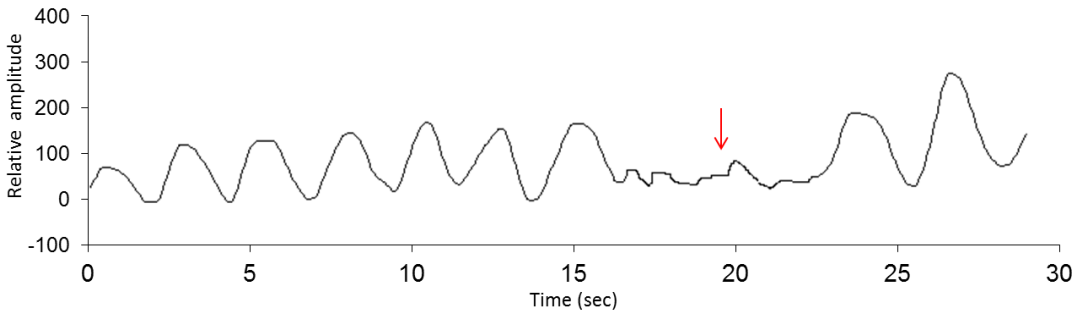

Figure 5.13 Sample respiratory signal of a patient indicated residual breathing (red arrow) during a breath-hold mediated by the ABC.

5.4.2 USE OF THE LOW CURRENT CT

We used tube current of 10 mA for the IACT acquisition because it was the lowest possible value on the current scanner. Even though the 10 mA CT images are much nosier than the conventional diagnostic CT images with a much higher current, they are still feasible for generating the IACT for AC in PET/CT. According to Xia et al. [81], the PET noise introduced by the ultra-low dose CT scans does not significantly affect the diagnostic information and the image quality of the associate attenuation-corrected PET. While IACT only imposed 0.38 mSv dose from two separate low dose HCT scans to each patient, the improvement of image quality and quantitative accuracy was substantial. Hence, CT dose can be reduced while it is mainly for AC and providing registered anatomical information, but may not be feasible for diagnostic purpose. Similar to the simulation study, the IACT for PET AC is relatively smoothed by averaging the extreme and interpolated images. Thus, extra smoothing for CT raw data was not performed before the IACT generation.

5.4.3 DUAL-TIME POINT EFFECT

The positioning of the ABC device was not feasible for the standard whole-body PET protocol. Thus, PET_{IACT} was done after the PET_{HCT} and concatenating the IACT into the standard whole-body HCT [26] was not a possible option in this study. The longer activity distribution time for thoracic PET acquisition may increase the lesion SUV [82] and overestimate the effectiveness of IACT. However, we found the average SUV_{mean} increase (32.9%) of the malignant lung tumors (n=9) in this study was substantially higher than the increased value (20.5%) as suggested by Matthies et al. who evaluated dual time point FDG PET for pulmonary nodules [78], even the delay between 2nd and 1st PET scan was just 30 mins as compared to ~60 mins in normal dual time point studies. Also, all benign lung lesions (n=5) showed obvious SUV increase in PET_{IACT} as compared to PET_{HCT}, although they do not usually demonstrate SUV increase in dual time point scans [78]. On the other hand, the lesion centroid differences between PET and associate CT confirmed the effectiveness of IACT (Table 5.2). In the future study, to cancel the potential delayed uptake effect, an

improved protocol will be implemented in which the thoracic IACT can be incorporated into the standard whole-body HCT directly to form a new composite whole-body CT dataset for whole-body PET reconstruction.

5.4.4 ACTUAL LESION MOTION EFFECTS ON IACT

The movement of the structures in the thorax is highly correlated to the diaphragm motion during the respiration [83]. Thus, in this paper, we utilized a diaphragmatic movement function (Equation 5.1) during the respiratory cycles to model the lesion movement pattern. Patients tend to spend more time towards the end-expiration period [84] and this can be reflected in the asymmetry of the respiratory signal. This degree of asymmetry was represented by an integer n in Equation 5.1, and can be determined for each patient specifically according to their acquired respiratory signal by calculating the elapsed time ratio between expiration and inspiration. Thus, our sinusoidal function for interpolation is indeed semi-patient specific. One may suggest using the full patient specific breathing signal for the interpolation function. Our preliminary study, however, showed that the quantitative difference of the PET results of using these two functions were negligible.

On the other hand, the B-spline method used in this study estimated the deformation vector of the lesion in three directions: superior-to-inferior, anterior-to-posterior and lateral. However, this combined vector may not indicate hysteresis where the lesion moving trajectories are not consistent from inspiration to expiration, or there may be some phase latency existed between the different tumor movement directions (e.g., superior-to-inferior and anterior-to-posterior). Hysteresis will induce a larger tumor volume size appeared in the PET images as compared to its real size, leading to the PET/CT misalignment. The lesions in the upper lung are more subject to the respiratory hysteresis, hence are more complicated to model as compared to the ones in the lower lung [85, 86]. The motion is even more complex with the lesions attached to the rigid structure in the thorax. In this study, we observed that only some of the lesions in the upper lung (patient#2) or attached to the ribcage (patient#10) had inferior mismatching in IACT-AC than using HCT-AC. So far, we

did not observe significant difference in terms of the quantification results for different thoracic regions which may because of the low number of lesions in each region. The preliminary results from our ongoing simulation study, however, showed that the improvement from IACT was more obvious for the lesions in the lower lung. Currently, we are investigating the effects of the lesion sizes, locations, uptake ratios and movement pattern on IACT effectiveness in both simulation and clinical study.

CHAPTER 6 : CONCLUSION AND FUTURE WORKS

Intrinsically fused PET and CT images from PET/CT provide more accurate lesion localization and characterization than separate PET and CT images. Many studies indicate that PET/CT has great potential in the staging of non-small cell lung cancer and lymph node cancer. Attenuation correction is the most important correction in PET and critical for improving image quality and quantitation. The CT-based method is better than the conventional ^{68}Ge-based transmission method for AC in PET in many aspects. However, it is hampered by respiratory artifacts. Several approaches to correct these artifacts in PET/CT images are summarized and compared in this thesis. The IACT is proposed as a new method to reduce the respiratory misalignments in PET/CT. CT images of the desired phases, e.g., end-inspiration and end-expiration phases from a respiratory cycle are used to generate the velocity matrix using deformable image registrations such as the OFM and B-spline algorithm. Interpolated phases are then obtained via linear and empirical/semi-patient specific sinusoidal functions. The IACT is obtained by averaging the original and interpolated phases.

In the simulation study, we have evaluated and analyzed the preliminary effectiveness of IACT as compared to CACT and HCT. The evaluation of IACT is set for a range of respiratory motion amplitudes and with realistic noisy simulations. The IACT modeled the respiratory motion similarly to the CACT method. Less artifacts and better mismatching were observed in the IACT-AC image compared to HCT-AC images. Quantitative measurements further proved the superiority and robustness of the proposed method in both noise-free and noisy simulations. We are currently investigating the effects of lesion sizes, lesion uptake ratios and lesion locations on the proposed methods and preliminary results showed that smaller lesions with lower TBR would be more challenging to model for IACT.

In the clinical study, we have developed an ABC prototype and evaluated the clinical feasibility of IACT-ABC method on patients with thoracic tumors. We showed that it potentially improved PET reconstructed image quality as compared to the conventional HCT, with reduced respiratory artifacts and spatial mismatch,

increased SUV of the lesions and lowered radiation dose. The IACT with the aid of ABC is a robust method for thoracic PET/CT AC, and is promising to improve the diagnostic accuracy of the thoracic tumors.

Based on the Chapter 2 and Chapter 5, we also made comparison between our method and conventional methods in terms of the clinical feasibility. IACT generation is automatically done with two registration processes, while gated 4D PET/CT may require multiple registrations. For CACT, there is no external respiratory monitoring device and breath-hold required for the acquisition, making it clinically more favorable. However, the dose reduction of IACT as compared to CACT is still substantial (0.38 mSv v.s. 2.36 mSv for 2 bed positions) from our former study.

Previously we applied the IACT for PET/CT cardiac scans and showed substantial image quality improvement on the reconstructed images [87]. Another cardiac viability/perfusion simulation study with IACT AC is ongoing and the preliminary results showed that IACT for cardiology application is promising. Further optimization of the IACT protocol with the consideration of dose reduction is warranted.

BIBLIOGRAPHY

[1] R. Siegel, D. Naishadham, and A. Jemal, "Cancer statistics, 2013," *CA-Cancer J. Clin.,* vol. 63, pp. 11-30, 2013.

[2] J. R. Molina, P. Yang, S. D. Cassivi, S. E. Schild, and A. A. Adjei, "Non-Small Cell Lung Cancer: Epidemiology, Risk Factors, Treatment, and Survivorship," *Mayo Clin. Proc.,* vol. 83, pp. 584-594, 2008.

[3] G. P. Kalemkerian, W. Akerley, P. Bogner, H. Borghaei, L. Chow, R. J. Downey, L. Gandhi, A. K. P. Ganti, R. Govindan, J. C. Grecula, J. Hayman, R. S. Heist, L. Horn, T. M. Jahan, M. Koczywas, C. A. Moran, H. B. Niell, J. O'Malley, J. D. Patel, N. Ready, C. M. Rudin, and C. C. Williams, "Small Cell Lung Cancer," *J. Natl. Compr. Canc. Netw.,* vol. 9, pp. 1086-1113, October 1, 2011 2011.

[4] D. Delbeke, R. E. Coleman, M. J. Guiberteau, M. L. Brown, H. D. Royal, B. A. Siegel, D. W. Townsend, L. L. Berland, J. A. Parker, K. Hubner, M. G. Stabin, G. Zubal, M. Kachelriess, V. Cronin, and S. Holbrook, "Procedure Guideline for Tumor Imaging with 18F-FDG PET/CT 1.0," *J. Nucl. Med.,* vol. 47, pp. 885-895, 2006.

[5] L. T. Chang, "A Method for Attenuation Correction in Radionuclide Computed Tomography " *IEEE. Trans. Nuc. Sci.,* vol. 25, pp. 638-643, 1978.

[6] M. Bergstrom, J. Litton, L. Eriksson, C. Bohm, and G. Blomqvist, "Determination of Object Contour from Projections for Attenuation Correction in Cranial Positron Emission Tomography," *J. Comput. Assist. Tomogr.,* vol. 6, pp. 365-372, 1982.

[7] S. R. Meikle, M. Dahlbom, and S. R. Cherry, "Attenuation Correction Using Count-Limited Transmission Data in Positron Emission Tomography," *J. Nucl. Med.,* vol. 34, pp. 143-144, 1993.

[8] P. E. Kinahan, B. H. Hasegawa, and T. Beyer, "X-ray-based attenuation correction for positron emission tomography/computed tomography scanners," *Semin. Nucl. Med.,* vol. 33, pp. 166-79, 2003.

[9] P. E. Kinahan, D. W. Townsend, T. Beyer, and D. Sashin, "Attenuation correction for a combined 3D PET/CT scanner," *Med. Phys.,* vol. 25, pp. 2046-2053, 1998.

[10] C. Burger, G. Goerres, S. Schoenes, A. Buck, A. Lonn, and G. von Schulthess, "PET attenuation coefficients from CT images: experimental evaluation of the transformation of CT into PET 511-keV attenuation coefficients," *Eur. J. Nucl. Med. Mol. Imaging.,* vol. 29, pp. 922-927, 2002.

[11] J. A. van Dalen, E. P. Visser, W. V. Vogel, F. H. M. Corstens, and W. J. G. Oyen, "Impact of Ge-68/Ga-68-based versus CT-based attenuation correction on PET," *Med. Phys.,* vol. 34, pp. 889-897, 2007.

[12] T. Beyer, G. Antoch, T. Blodgett, L. F. Freudenberg, T. Akhurst, and S. Mueller, "Dual-modality PET/CT imaging: the effect of respiratory motion on combined image quality in clinical oncology," *Eur. J. Nucl. Med. Mol. Imaging.,* vol. 30, pp. 588-596, 2003.

[13] M. M. Osman, C. Cohade, Y. Nakamoto, and R. L. Wahl, "Respiratory motion artifacts on PET emission images obtained using CT attenuation correction on PET-CT," *Eur. J. Nucl. Med. Mol. Imaging.,* vol. 30, pp. 603-606, 2003.

[14] W. Sureshbabu and O. Mawlawi, "PET/CT Imaging Artifacts," *J. Nucl. Med. Technol.,* vol. 33, pp. 156-161, 2005.

[15] T. Beyer, A. Bockisch, H. Kühl, and M.-J. Martinez, "Whole-Body 18F-FDG PET/CT in the Presence of Truncation Artifacts," *J. Nucl. Med.,* vol. 47, pp. 91-99, 2006.

[16] G. W. Goerres, F. Hany, E. Kamel, G. K. von Schulthess, and A. Buck, "Head and neck imaging with PET and PET/CT: artefacts from dental metallic implants," *Eur. J. Nucl. Med. Mol. Imaging.,* vol. 29, pp. 367-370, 2002.

[17] E. M. Kamel, C. Burger, A. Buck, G. K. von Schulthess, and G. W. Goerres, "Impact of metallic dental implants on CT-based attenuation correction in a combined PET/CT scanner," *Eur. Radiol.,* vol. 13, pp. 724-728, 2003.

[18] G. Antoch, L. S. Freudenberg, T. Egelhof, J. Stattaus, W. Jentzen, J. F. Debatin, and A. Bockisch, "Focal Tracer Uptake: A Potential Artifact in Contrast-Enhanced Dual-Modality PET/CT Scans," *J. Nucl. Med.,* vol. 43, pp. 1339-1342, 2002.

[19] E. Dizendorf, T. F. Hany, A. Buck, G. K. von Schulthess, and C. Burger, "Cause and magnitude of the error induced by oral CT contrast agent in CT-based attenuation correction of PET emission studies," *J. Nucl. Med.,* vol. 44, pp. 732-738, 2003.

[20] K. L. Gould, T. Pan, C. Loghin, N. P. Johnson, A. Guha, and S. Sdringola, "Frequent diagnostic errors in cardiac PET/CT due to misregistration of CT attenuation and emission PET images: a definitive analysis of causes, consequences, and corrections," *J. Nucl. Med.,* vol. 48, pp. 1112-21, 2007.

[21] G. Cook, E. Wegner, and I. Fogelman, "Pitfalls and artifacts in FDG PET and PET/CT oncologic imaging," *Semin. Nucl. Med.,* vol. 34, pp. 122-133, 2004.

[22] S. A. Nehmeh and Y. E. Erdi, "Respiratory Motion in Positron Emission Tomography/Computed Tomography: A Review," *Semin. Nucl. Med.,* vol. 38, pp. 167-176, 2008.

[23] R. Juan, B. Seifert, T. Berthold, G. Schulthess, and G. Goerres, "Clinical evaluation of a breathing protocol for PET/CT," *Eur. Radiol.,* vol. 14, pp. 1118-1123, 2004.

[24] G. W. Goerres, E. Kamel, B. Seifert, C. Burger, A. Buck, T. F. Hany, and G. K. von Schulthess, "Accuracy of Image Coregistration of Pulmonary Lesions in Patients with Non-Small Cell Lung Cancer Using an Integrated PET/CT System," *J. Nucl. Med.,* vol. 43, pp. 1469-1475, 2002.

[25] T. Pan, O. Mawlawi, S. A. Nehmeh, Y. E. Erdi, D. Luo, H. H. Liu, R. Castillo, R. Mohan, Z. Liao, and H. A. Macapinlac, "Attenuation Correction of PET Images with Respiration-Averaged CT Images in PET/CT," *J. Nucl. Med.,* vol. 46, pp. 1481-1487, 2005.

[26] T. Pan, O. Mawlawi, D. Luo, H. H. Liu, P.-c. M. Chi, M. V. Mar, G. Gladish, M. Truong, J. Erasmus, Z. Liao, and H. A. Macapinlac, "Attenuation correction of PET cardiac data with low-dose average CT in PET/CT," *Med. Phys.,* vol. 33, pp. 3931-3938, 2006.

[27] A. M. Alessio, S. Kohlmyer, K. Branch, G. Chen, J. Caldwell, and P. Kinahan, "Cine CT for Attenuation Correction in Cardiac PET/CT," *J. Nucl. Med.,* vol. 48, pp. 794-801, 2007.

[28] C. C. A. Nagel, G. Bosmans, A. L. A. J. Dekker, M. C. Ollers, D. K. M. D. Ruysscher, P. Lambin, A. W. H. Minken, N. Lang, and K. P. Schafers, "Phased attenuation correction in respiration correlated computed tomography/positron emitted tomography," *Med. Phys.,* vol. 33, pp. 1840-1847, 2006.

[29] N. Grotus, A. J. Reader, S. Stute, J. C. Rosenwald, P. Giraud, and I. Buvat, "Fully 4D list-mode reconstruction applied to respiratory-gated PET scans," *Phys. Med. Biol.,* vol. 54, pp. 1705-1721, 2009.

[30] R. G. Wells, T. D. Ruddy, R. A. DeKemp, J. N. DaSilva, and R. S. Beanlands, "Single-Phase CT Aligned to Gated PET for Respiratory Motion Correction in Cardiac PET/CT," *J. Nucl. Med.,* vol. 51, pp. 1182-1190, 2010.

[31] C. Liu, A. Alessio, L. Pierce, K. Thielemans, S. Wollenweber, A. Ganin, and P. Kinahan, "Quiescent period respiratory gating for PET/CT," *Med. Phys.,* vol. 37, pp. 5037-5043, 2010.

[32] S. J. McQuaid, T. Lambrou, and B. F. Hutton, "A novel method for incorporating respiratory-matched attenuation correction in the motion correction of cardiac PET–CT studies," *Phys. Med. Biol.,* vol. 56, pp. 2903-2915, 2011.

[33] S. A. Nehmeh, Y. E. Erdi, T. Pan, A. Pevsner, K. E. Rosenzweig, E. Yorke, G. S. Mageras, H. Schoder, P. Vernon, O. Squire, H. Mostafavi, S. M. Larson, and J. L. Humm, "Four-dimensional (4D) PET/CT imaging of the thorax," *Med. Phys.,* vol. 31, pp. 3179-3186, 2004.

[34] I. E. Naqa, D. A. Low, J. D. Bradley, M. Vicic, and J. O. Deasy, "Deblurring of breathing motion artifacts in thoracic PET images by deconvolution methods," *Med. Phys.,* vol. 33, pp. 3587-3600, 2006.

[35] G. Chang, T. Chang, T. Pan, J. John W. Clark, and O. R. Mawlawi, "Joint correction of respiratory motion artifact and partial volume effect in lung/thoracic PET/CT imaging," *Med. Phys.,* vol. 37, pp. 6221-6232, 2010.

[36] M. Allen-Auerbach, K. Yeom, J. Park, M. Phelps, and J. Czernin, "Standard PET/CT of the Chest During Shallow Breathing Is Inadequate for Comprehensive Staging of Lung Cancer," *J. Nucl. Med.,* vol. 47, pp. 298-301, 2006.

[37] T. Beyer, S. Rosenbaum, P. Veit, J. Stattaus, S. P. Muller, F. P. Difilippo, H. Schoder, O. Mawlawi, F. Roberts, A. Bockisch, and H. Kuhl, "Respiration artifacts in whole-body (18)F-FDG PET/CT studies with combined PET/CT tomographs employing spiral CT technology with 1 to 16 detector rows," *Eur. J. Nucl. Med. Mol. Imaging.,* vol. 32, pp. 1429-39, 2005.

[38] R. de Juan, B. Seifert, T. Berthold, G. K. von Schulthess, and G. W. Goerres, "Clinical evaluation of a breathing protocol for PET/CT," *Eur. Radiol.,* vol. 14, pp. 1118-1123, 2004.

[39] J. J. Hamill, G. Bosmans, and A. Dekker, "Respiratory-gated CT as a tool for the simulation of breathing artifacts in PET and PET/CT," *Med. Phys.,* vol. 35, pp. 576-585, 2008.

[40] S. A. Nehmeh, Y. E. Erdi, G. S. P. Meirelles, O. Squire, S. M. Larson, J. L. Humm, and H. Schöder, "Deep-Inspiration Breath-Hold PET/CT of the Thorax," *J. Nucl. Med.,* vol. 48, pp. 22-26, 2007.

[41] G. S. P. Meirelles, Y. E. Erdi, S. A. Nehmeh, O. D. Squire, S. M. Larson, J. L. Humm, and H. Schoder, "Deep-inspiration breath-hold PET/CT: clinical findings with a new technique for detection and characterization of thoracic lesions," *J. Nucl. Med.,* vol. 48, pp. 712-9, May 2007.

[42] T. Torizuka, Y. Tanizaki, T. Kanno, M. Futatsubashi, E. Yoshikawa, H. Okada, and Y. Ouchi, "Single 20-Second Acquisition of Deep-Inspiration Breath-Hold PET/CT: Clinical Feasibility for Lung Cancer," *J. Nucl. Med.,* vol. 50, pp. 1579-1584, 2009.

[43] W. A. Kalender, W. Seissler, E. Klotz, and P. Vock, "Spiral volumetric CT with single-breath-hold technique, continuous transport, and continuous scanner rotation," *Radiology,* vol. 176, pp. 181-183, 1990.

[44] W. A. Kalender, "X-ray computed tomography," *Phys. Med. Biol.,* vol. 51, p. R29, 2006.

[45] F. J. Lagerwaard, J. R. Van Sornsen de Koste, M. R. J. Nijssen-Visser, R. H. Schuchhard-Schipper, S. S. Oei, A. Munne, and S. Senan, "Multiple "slow" CT scans for incorporating lung tumor mobility in radiotheraphy planning," *Int. J. Radiat. Oncol. Biol. Phys.,* vol. 51, pp. 932-937, 2001.

[46] J. A. Nye, F. Esteves, and J. R. Votaw, "Minimizing artifacts resulting from respiratory and cardiac motion by optimization of the transmission scan in cardiac PET/CT," *Med. Phys.,* vol. 34, pp. 1901-1906, 2007.

[47] T. Pan, T.-Y. Lee, E. Rietzel, and G. T. Y. Chen, "4D-CT imaging of a volume influenced by respiratory motion on multi-slice CT," *Med. Phys.,* vol. 31, pp. 333-240, 2004.

[48] R. A. Cook, G. Carnes, T. Y. Lee, and R. G. Wells, "Respiration-averaged CT for attenuation correction in canine cardiac PET/CT," *J. Nucl. Med.,* vol. 48, pp. 811-8, May 2007.

[49] Picard Y and T. CJ, "Motion Correction of PET Images Using Multiple Acquisition Frames," *IEEE. Trans. Med. Imaging.,* vol. 16, pp. 137-44, 1997.

[50] S. A. Nehmeh, Y. E. Erdi, C. C. Ling, K. E. Rosenzweig, O. D. Squire, L. E. Braban, E. Ford, K. Sidhu, G. S. Mageras, S. M. Larson, and J. L. Humm, "Effect of respiratory gating on reducing lung motion artifacts in PET imaging of lung cancer," *Med. Phys.,* vol. 29, pp. 366-371, 2002.

[51] M. Dawood, F. Buther, J. Xiaoyi, and K. P. Schafers, "Respiratory Motion Correction in 3-D PET Data With Advanced Optical Flow Algorithms," *IEEE. Trans. Med. Imaging.,* vol. 27, pp. 1164-1175, 2008.

[52] B. Thorndyke, E. Schreibmann, A. Koong, and L. Xing, "Reducing respiratory motion artifacts in positron emission tomography through retrospective stacking," *Med. Phys.,* vol. 33, p. 2632, 2006.

[53] M. Soret, S. L. Bacharach, and I. Buvat, "Partial-Volume Effect in PET Tumor Imaging," *J. Nucl. Med.,* vol. 48, pp. 932-945, June 2007 2007.

[54] D. Visvikis, F. Lamare, P. Bruyant, N. Boussion, and C. Cheze Le Rest, "Respiratory motion in positron emission tomography for oncology

applications: Problems and solutions," *Nucl. Instrum. Meth. A,* vol. 569, pp. 453-457, 2006.

[55] F. Lamare, M. J. L. Carbayo, T. Cresson, G. Kontaxakis, A. Santos, C. C. L. Rest, A. J. Reader, and D. Visvikis, "List-mode-based reconstruction for respiratory motion correction in PET using non-rigid body transformations," *Phys. Med. Biol.,* vol. 52, pp. 5187-5204, 2007.

[56] T. Li, B. Thorndyke, E. Schreibmann, Y. Yang, and L. Xing, "Model-based image reconstruction for four-dimensional PET," *Med. Phys.,* vol. 33, pp. 1288-1298, 2006.

[57] F. Qiao, T. Pan, J. W. C. Jr, and O. R. Mawlawi, "A motion-incorporated reconstruction method for gated PET studies," *Phys. Med. Biol.,* vol. 51, pp. 3769-3783, 2006.

[58] J. Ming, W. Ge, M. W. Skinner, J. T. Rubinstein, and M. W. Vannier, "Blind deblurring of spiral CT images," *IEEE. Trans. Med. Imaging.,* vol. 22, pp. 837-845, 2003.

[59] S. Sourbron, R. Luypaert, P. Van Schuerbeek, M. Dujardin, T. Stadnik, and M. Osteaux, "Deconvolution of dynamic contrast-enhanced MRI data by linear inversion: Choice of the regularization parameter," *Magn. Reson. Med.,* vol. 52, pp. 209-213, 2004.

[60] A. S. Kirov, J. Z. Piao, and C. R. Schmidtlein, "Partial volume effect correction in PET using regularized iterative deconvolution with variance control based on local topology," *Phys. Med. Biol.,* vol. 53, pp. 2577-2591, 2008.

[61] T. L. Faber, N. Raghunath, D. Tudorascu, and J. R. Votaw, "Motion correction of PET brain images through deconvolution: I. Theoretical development and analysis in software simulations," *Phys. Med. Biol.,* vol. 54, pp. 797-811, 2009.

[62] B. K. P. Horn and B. G. Schunck, "Determining Optical Flow," Massachusetts Institute of Technology,1980.

[63] H. Tzung-Chi, G. S. P. Mok, S.-J. Wang, T.-H. Wu, and G. Zhang, "Attenuation correction of PET images with interpolated average CT for thoracic tumors," *Phys. Med. Biol.,* vol. 56, pp. 2559-2567, 2011.

[64] Z. Wu, E. Rietzel, V. Boldea, D. Sarrut, and G. C. Sharp, "Evaluation of deformable registration of patient lung 4DCT with subanatomical region segmentations," *Med. Phys.,* vol. 35, pp. 775-781, 2008.

[65] D. Rueckert, L. I. Sonoda, C. Hayes, D. L. G. Hill, M. O. Leach, and D. J. Hawkes, "Nonrigid registration using free-form deformations: application to breast MR images," *IEEE. Trans. Med. Imaging.,* vol. 18, pp. 712-721, 1999.

[66] T. Rohlfing and C. R. Maurer, Jr., "Nonrigid image registration in shared-memory multiprocessor environments with application to brains, breasts, and bees," *IEEE. Trans. Inf. Technol. B.,* vol. 7, pp. 16-25, 2003.

[67] G. Wahba, "Spline Models for Observational Data," *Society for Industrial and Applied Mathematics. CBMS-NSF Regional Conf. series in applied mathematics,* 1990.

[68] W. P. Segars, D. S. Lalush, and B. M. W. Tsui, "Modeling respiratory mechanics in the MCAT and spline-based MCAT phantoms," *IEEE. Trans. Nucl. Sci.,* vol. 48, pp. 89-97, 2001.

[69] A. E. Lujan, J. M. Balter, and R. K. T. Haken, "A method for incorporating organ motion due to breathing into 3D dose calculations in the liver: Sensitivity to variations in motion," *Med. Phys.,* vol. 30, pp. 2643-2649, 2003.

[70] G. S. P. Mok, S. Tao, H. Tzung-Chi, and M. I. Vai, "Interpolated Average CT for Attenuation Correction in PET-A Simulation Study," *IEEE. Trans. Bio-Med. Eng.,* vol. 60, pp. 1927-1934, 2013.

[71] T. Kris, T. Charalampos, M. Sanida, B. Tobias, A. Pablo, D. Nikolaos, and W. J. Matthew, "STIR: software for tomographic image reconstruction release 2," *Phys. Med. Biol.,* vol. 57, p. 867, 2012.

[72] A. Pevsner, S. A. Nehmeh, J. L. Humm, G. S. Mageras, and Y. E. Erdi, "Effect of motion on tracer activity determination in CT attenuation corrected PET images: A lung phantom study," *Med. Phys.,* vol. 32, pp. 2358-2362, 2005.

[73] J. W. Wong, M. B. Sharpe, D. A. Jaffray, V. R. Kini, J. M. Robertson, J. S. Stromberg, and A. A. Martinez, "The use of active breathing control (ABC) to reduce margin for breathing motion," *Int. J. Radiat. Oncol. Biol. Phys.,* vol. 44, pp. 911-919, 1999.

[74] T. Sun, T.-H. Wu, S.-J. Wang, B.-H. Yang, N.-Y. Wu, and G. S. P. Mok, "Low dose interpolated average CT for thoracic PET/CT attenuation correction using an active breathing controller," *Med. Phys.,* vol. 40, pp. 102507-9, 2013.

[75] T. S. Yoo, M. J. Ackerman, and W. E. Lorensen, "Engineering and algorithm design for an image processing API: A technical report on itk-the insight toolkit," *Proc. of Medicine Meets Virtual Reality,* pp. 586-592, 2002.

[76] R. Boellaard, M. O'Doherty, W. Weber, F. Mottaghy, M. Lonsdale, S. Stroobants, W. G. Oyen, J. Kotzerke, O. Hoekstra, J. Pruim, P. Marsden, K. Tatsch, C. Hoekstra, E. Visser, B. Arends, F. Verzijlbergen, J. Zijlstra, E. I. Comans, A. Lammertsma, A. Paans, A. Willemsen, T. Beyer, A. Bockisch, C. Schaefer-Prokop, D. Delbeke, R. Baum, A. Chiti, and B. Krause, "FDG PET and PET/CT: EANM procedure guidelines for tumour PET imaging: version 1.0," *Eur. J. Nucl. Med. Mol. Imaging,* vol. 37, pp. 181-200, 2010.

[77] K. Mah, C. B. Caldwell, Y. C. Ung, C. E. Danjoux, J. M. Balogh, S. N. Ganguli, L. E. Ehrlich, and R. Tirona, "The impact of 18 FDG-PET on target and critical organs in CT-based treatment planning of patients with poorly defined non-small-cell lung carcinoma: a prospective study," *Int. J. Radiat. Oncol.,* vol. 52, pp. 339-350, 2002.

[78] A. Matthies, M. Hickeson, A. Cuchiara, and A. Alavi, "Dual Time Point 18F-FDG PET for the Evaluation of Pulmonary Nodules," *J. Nucl. Med.,* vol. 43, pp. 871-875, 2002.

[79] L. Fin, J. Daouk, J. Morvan, P. Bailly, I. Esper, L. Saidi, and M.-E. Meyer, "Initial clinical results for breath-hold CT-based processing of respiratory-gated PET acquisitions," *Eur. J. Nucl. Med. Mol. Imaging,* vol. 35, pp. 1971-1980, 2008.

[80] G. Bongartz, S.J. Golding, A.G. Jurik, M. Leonardi, E. van Persijn van Meerten, R. Rodríguez, K. Schneider, A. Calzado, J. Geleijns, K.A. Jessen, W. Panzer, P. C. Shrimpton, and G. Tosi, *European Guidelines for Multislice Computed Tomography,* Brussels, Belgium: European Commission, 2004: FIGM-CT2000-20078-CT-TIP.

[81] T. Xia, A. M. Alessio, B. De Man, R. Manjeshwar, E. Asma, and P. E. Kinahan, "Ultra-low dose CT attenuation correction for PET/CT," *Phys. Med. Biol.,* vol. 57, pp. 309-28, 2012.

[82] S. Basu, H. Zaidi, S. Holm, and A. Alavi, "Quantitative Techniques in PET-CT Imaging," *Curr. Med. Imag. Rev.,* vol. 7, pp. 216-233, 2011.

[83] L. I. Cervino, A. K. Chao, A. Sandhu, and S. B. Jiang, "The diaphragm as an anatomic surrogate for lung tumor motion," *Phys. Med. Biol.,* vol. 54, pp. 3529-41, 2009.

[84] C. Liu, L. A. P. II, A. M. Alessio, and P. E. Kinahan, "The impact of respiratory motion on tumor quantification and delineation in static PET/CT imaging," *Phys. Med. Biol.,* vol. 54, pp. 7345-7362, 2009.

[85] Y. Seppenwoolde, H. Shirato, K. Kitamura, S. Shimizu, M. van Herk, J. V. Lebesque, and K. Miyasaka, "Precise and real-time measurement of 3D tumor motion in lung due to breathing and heartbeat, measured during radiotherapy," *Int. J. Radiat. Oncol.,* vol. 53, pp. 822-834, 2002.

[86] V. Boldea, G. C. Sharp, S. B. Jiang, and D. Sarrut, "4D-CT lung motion estimation with deformable registration: Quantification of motion nonlinearity and hysteresis," *Med. Phys.,* vol. 35, pp. 1008-1018, 2008.

[87] T.-H. Wu, G. Zhang, S.-J. Wang, C.-H. Chen, B.-H. Yang, N.-Y. Wu, and T.-C. Huang, "Low-dose interpolated average CT for attenuation correction in cardiac PET/CT," *Nucl. Instrum. Meth. A,* vol. 619, pp. 361-364, 2010.

Vita

Sun Tao

Education Background:

2006/06-2010/07: Tianjin University, Tianjin, China.
B.E. in Electronic Information Engineering

Publications:

Journal Publications

Sun T**,** Wu TH, Wang SJ, Yang BH, Wu NY, Mok GSP. "Low dose interpolated average CT for thoracic PET/CT attenuation correction using an active breathing controller (ABC)". Medical Physics, vol.40, pp.102507, 2013.

Mok GSP, Sun T, Huang TC, Vai MI. "Interpolated Average CT for Attenuation Correction in PET – a Simulation Study". IEEE Transaction on Biomedical Engineering, vol. 60:7, pp. 1927-1934, 2013.

Sun T,Mok GSP, "Techniques for respiration-induced artifacts reductions in thoracic PET/CT". Quantitative Imaging in Medicine and Surgery, vol. 2, pp. 46-52, 2012.

Conference Presentations and Records

Ho CYT, Sun T, Wu TH, Mok GSP**. "**Performance Evaluation of Interpolated Average CT for PET Attenuation Correction in Different Lesion Characteristics". Abstract accepted for presentation in IEEE Nuclear Science Symposium and Medical Imaging Conference, Seoul, Korea, 2013.

Mok GSP, Ho C, Sun T. "Interpolated Average CT for Reducing Cardiac PET/CT Artifacts". Abstract accepted for presentation in 2013 Annual Congress of the European Association of Nuclear Medicine, Lyon, France, 2013.

Mok GSP, Sun T, Wang SJ, Wu TH. "Clinical evaluation of interpolated average CT using active breathing controller (ABC) for attenuation correction in thoracic PET/CT". Paper presented in Society of Nuclear Medicine and Molecular Imaging 2013 Annual Meeting, Vancouver, Canada, 2013.

Mok GSP, Ho C, Sun T. "Interpolated average CT for cardiac PET/CT attenuation correction - a simulation study". Paper presented in Society of Nuclear Medicine and Molecular Imaging 2013 Annual Meeting, Vancouver, Canada, 2013.

Sun T, Wu TH, Wu NY, Mok GSP. "Low Dose Interpolated Average CT for PET/CT Attenuation Correction Using an Active Breathing Controller (ABC)". Oral presentation in IEEE Nuclear Science Symposium and Medical Imaging Conference, Anaheim, USA, 2012.

Mok GSP, Sun T, Wu TH, Chang MB, Huang TC. "Interpolated Average CT for Attenuation Correction in PET – a Simulation Study". Paper presented in IEEE Nuclear Science Symposium and Medical Imaging Conference, Valencia, Spain, 2011.

Book Chapter

Mok GSP, Sun T, Liu C. "Reducing respiratory artifacts in thoracic PET/CT". Book chapter in Medical Imaging: Technology and Applications, CRC Press,
Published: October 1, 2013 by CRC Press - 732 Pages